Dissociative electron attachment to the H_2O molecule. II. Nuclear dynamics on coupled electronic surfaces within the local complex potential model

Daniel J. Haxton,[1,2,*] T. N. Rescigno,[2] and C. W. McCurdy[2,3]
[1]*Department of Chemistry, University of California, Berkeley, California 94720, USA*
[2]*Lawrence Berkeley National Laboratory, Chemical Sciences, Berkeley, California 94720, USA*
[3]*Departments of Applied Science and Chemistry, University of California, Davis, California 95616, USA*
(Received 1 December 2006; published 16 January 2007)

We report the results of a first-principles study of dissociative electron attachment to H_2O. The cross sections were obtained from nuclear dynamics calculations carried out in full dimensionality within the local complex potential model by using the multiconfiguration time-dependent Hartree method. The calculations employ our previously obtained global, complex-valued, potential-energy surfaces for the three ($^2B_1$, $^2A_1$, and $^2B_2$) electronic Feshbach resonances involved in this process. These three metastable states of H_2O^- undergo several degeneracies, and we incorporate both the Renner-Teller coupling between the $^2B_1$ and $^2A_1$ states as well as the conical intersection between the $^2A_1$ and $^2B_2$ states into our treatment. The nuclear dynamics are inherently multidimensional and involve branching between different final product arrangements as well as extensive excitation of the diatomic fragment. Our results successfully mirror the qualitative features of the major fragment channels observed, but are less successful in reproducing the available results for some of the minor channels. We comment on the applicability of the local complex potential model to such a complicated resonant system.

DOI: 10.1103/PhysRevA.75.012711 PACS number(s): 34.80.Ht

I. INTRODUCTION

In the preceding paper [1], referred to hereafter as paper I, we presented global representations of the three ($^2B_1$, $^2A_1$, and $^2B_2$) complex-valued potential-energy surfaces of the metastable states of H_2O^-, which underlie dissociative electron attachment to water. This paper is concerned with the calculation of the cross sections for that physical process. Prior experimental and theoretical results [2–20] have characterized the various breakup channels and determined the spatial symmetries of the three metastable electronic states of H_2O^-, the $^2B_1$, $^2A_1$, and $^2B_2$electronic Feshbach resonances, which are responsible for production of H^- and O^-. As explained in Ref. [18] and paper I, the energetically lowest $H+OH^-$ channel does not directly correlate with any of the three Feshbach states. We therefore conclude that OH^- production must be due to nonadiabatic effects.

We pursue this problem theoretically using a coupled Born-Oppenheimer treatment of the nuclear motion. The first task, which was described in paper I, is the construction of three-dimensional, complex-valued potential-energy surfaces for these three states, which have a negative imaginary component due to the finite probability of electron autodetachment back to H_2O+e^-. These complex-valued potential-energy surfaces, which are functions of the nuclear geometry $\vec{q}$, are defined as

$$V(\vec{q}) = E_R(\vec{q}) - i\frac{\Gamma(\vec{q})}{2}, \tag{1}$$

where E_R is the resonance position and Γ is the width of the resonance, which is related to the lifetime by $\tau=1/\Gamma$. (We use atomic units throughout this paper.) The present paper, which we label paper II, is concerned with the use of these potential curves within the local complex potential (LCP) model [21–25] to calculate the nuclear dynamics leading to dissociation. The analysis of the dynamics yields the dissociative electron attachment (DEA) cross section as a function of incident electron energy.

We must account for two major nonadiabatic physical effects in calculating the quantum dynamics of the nuclei. As described in paper I, the three potential-energy surfaces have several degeneracies that lead to coupling among them. First, the $^2B_1$ and $^2A_1$ states become members of a degenerate $^2\Pi$ pair in linear geometry, and for this reason there will be Renner-Teller coupling between them. We expect this coupling to be relevant for DEA via the $^2A_1$ state, because the gradient of its potential-energy surface will cause the system to move toward linear geometry after the electron attaches. Second, there is a conical intersection [18] between the $^2B_2$ and $^2A_1$ states that leads to coupling between them. For this reason, as described in paper I, we constructed a set of diabatic $^2B_2$ and $^2A_1$ surfaces, along with a coupling term, which we use in the calculations presented in this paper.

In Fig. 1, we show the real parts E_R of the constructed potential-energy surfaces along a two-dimensional cut, which includes the equilibrium geometry of the neutral ($r_1=r_2=1.81a_0$; $\theta_{HOH}=104.5°$). The degeneracies that lead to the nonadiabatic effects listed above can be seen in this figure. The two-dimensional cut depicted is that for which the two OH bond lengths are equal ($r_1=r_2$), corresponding to C_{2v} symmetry. (In C_{2v} symmetry, the adiabatic and diabatic $^2A_1$ and $^2B_2$ surfaces coincide.) The backside of this cut lies at $r_1=r_2=1.81a_0$, which is the equilibrium value of the bond lengths in neutral H_2O, and is marked with solid lines. The surfaces extend forward in Fig. 1 along the symmetric stretch direction to geometries at which $r_1=r_2=2.7a_0$. The conical

*Present address: Department of Physics and JILA, University of Colorado, Boulder, CO 80309, USA.

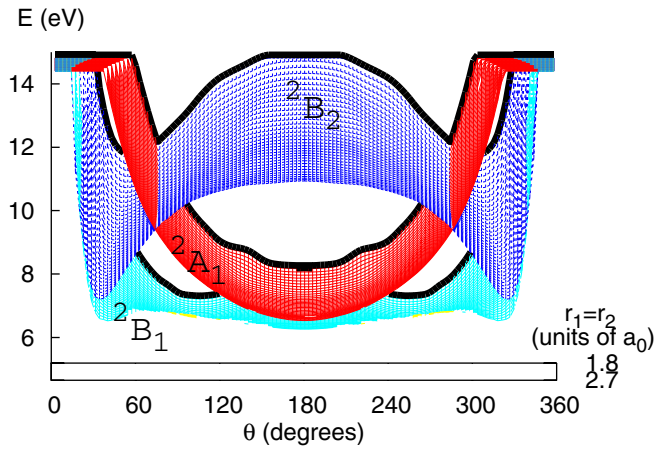

FIG. 1. (Color online) Real parts of resonance energies E_R as constructed in paper I within C_{2v} geometry ($r_1=r_2$), plotted with respect to bending angle and symmetric stretch distance.

intersection comprises the set of points along which the $^2A_1$ and $^2B_2$ surfaces intersect. The Renner-Teller degeneracy between the $^2B_1$ and $^2A_1$ states occurs at $\theta=180°$.

Although Fig. 1 shows only one cut of the potential-energy surfaces, and only their real part, it is useful for introducing certain features of these surfaces and the dynamics that will result. Dissociative attachment via the lower $^2B_1$ and $^2A_1$ states leads primarily to the product H^-+OH ($X^2\Pi$). The two OH bond lengths for such an arrangement are unequal, and therefore this product arrangement cannot be seen in Fig. 1. However, we can see that at the equilibrium geometry of the neutral, the $^2B_1$ surface is relatively flat with bend, while the $^2A_1$ surface slopes steeply downward toward linear geometry ($\theta=180°$). As a result, the dynamics beginning on the $^2A_1$ surface will lead toward linear geometry, and we expect that the Renner-Teller coupling between these two states will be more important for DEA via the $^2A_1$ than via the $^2B_1$ state.

The channel H_2+O^- is the minor channel for DEA via the $^2B_1$ and $^2A_1$ states, but the major channel for the $^2B_2$ state. We can see why this is the case from Fig. 1; the gradient of the $^2B_2$ ($2^2A'$) surface leads downward from the ground-state equilibrium geometry toward the conical intersection, where the system may make a nonadiabatic transition to the lower surface and access the clearly visible H_2+O^- well on the 1 $^2A'$ (lower cone) surface. The 2 $^2A'$ surface does not have a low-energy asymptote in this geometry, instead correlating to O^-+H_2 ($\sigma_g^1\sigma_u^1$).

The outline of this paper is as follows. In Sec. II, we summarize previous experimental and theoretical work on this problem. In Sec. III, we present the local complex potential model, which forms the foundation of our theoretical implementation. The Hamiltonian for the rovibrational nuclear motion of a triatomic molecule, and the additional terms that arise when the Renner-Teller effect is included, are described in Sec. IV. In Sec. V we describe the multiconfiguration time-dependent Hartree (MCTDH) method, which we use to calculate the nuclear dynamics, and the formalism for calculating the DEA cross sections. In Sec. VI, we present the final results of this study: cross sections, as a function of incident electron energy, resolved into the final rovibrational product states.

II. PREVIOUS EXPERIMENTAL AND THEORETICAL RESULTS

Dissociative electron attachment to water molecules has been the subject of previous experimental investigation, starting as early as 1930 [2], and as recently as the past year (2006) [20]. Early experiments on dissociative electron attachment to H_2O focused mainly on the identification of the negative ion species formed, the measurement of the total cross sections, and the energy locations of the structures in the resonance process [6]. Buchel'nikova [3] and Schultz [4] established that the main products of dissociative electron attachment to water are H^- and O^-, with the production of O^- being almost ten times smaller than that of H^- at lower energies, but with O^- dominating at higher electron-impact energies.

Both Compton and Christophorou [5] and Melton [6] carried out comprehensive studies of negative ion formation in water and measured absolute cross sections for DEA. Three resonance peaks were observed. H^- production was observed at approximately 6.5 and 8.6 eV, with the second peak much less intense than the first. The species O^- was observed in increasing intensities in three peaks at 7.0, 9.0, and 11.8 eV [5].

The species OH^- is also observed in the dissociative electron attachment experiments, though at an intensity one order of magnitude below the minor O^-+H_2 channel, which is itself observed at an intensity approximately one order of magnitude lower than the dominant H^-+OH channel. Melton [6] argued that OH^-+H was a true channel of dissociative electron attachment to H_2O molecules, while in subsequent studies (e.g., Ref. [26]) it was argued that OH^- is produced by DEA to water clusters $[H_2O]_n$. The question of OH^- production has been reexamined in the recent experimental study of Fedor *et al.* [20]. These authors have concluded that, indeed, it is a direct product of dissociative electron attachment to water. This minor channel is not examined in the present treatment, and no mechanism has, as yet, been advanced.

The effects of isotopic substitution have also been an issue of some debate. The replacement of H_2O by D_2O as the molecular target has the effect of nearly doubling the reduced masses corresponding to OH (OD) bond motion. One would expect, at least in a simple one-dimensional picture, that the nuclear dynamics may be substantially altered by such replacement, and in particular, the time to dissociation is increased. A longer dissociation time allows a greater amount of electron autodetachment to take place; therefore, performing the same experiment with different isotopic variants provides information on the lifetime of the electronic state involved. The cross sections for DEA via both H_2O and D_2O were measured, compared, and discussed in detail by Compton and Christophoreau [5]. A smaller peak cross section for D^- production than for H^- production via the lowest-energy $^2B_1$ state was observed. On the basis of these results, these authors derived an approximate lifetime of 2.1×10^{-14} s for

the lowest-energy $^2B_1$ Feshbach resonance. We published an initial study of DEA via this state [16], which arrived at results and conclusions much different from those of Ref. [5]. The calculated results yielded a higher peak cross section for D^- production via the $^2B_1$ resonance than for H^- production, and a similar energy-integrated cross section, in stark contrast to the results of Compton [5]. The calculations indicated a larger lifetime of 10.9×10^{-14} s for the $^2B_1$ state, and the nuclear dynamics that we calculated indicated that only a small portion of the dissociating anion flux is lost to autodetachment.

The recent experimental results of Fedor *et al.* [20] have substantially resolved this controversy. These authors obtain results different from those of Ref. [5], reversing the trend in peak heights for H^- versus D^- production via the $^2B_1$ resonance. They observe a higher peak for D^- production than for H^- production, which brings the current experimental and theoretical results into qualitative agreement.

Although the peak heights provide considerable information about the physical process of dissociative electronic attachment to water, further information is gained by resolving the angular dependence of the fragments produced, and the final (ro)vibrational state of the diatomic fragment. A series of measurements by Trajmar and Hall [8] and Belic, Laudau, and Hall [9] revealed the energy and angular dependence of H^- in dissociative electron attachment to H_2O. The determination of the angular dependence aided the assignment of the spatial symmetries of the three resonant states, B_1, A_1, and B_2, which had previously been misassigned. By resolving the kinetic energy of the H^- fragment, this experiment yielded information about the vibrational and rotational state distribution of the OH fragments.

Curtis and Walker [10] measured cross sections for dissociative electron attachment to D_2O and obtained two important results. By measuring the kinetic energy of recoil of the D^- fragments produced, these researchers established that both ground-state OD ($^2\Pi$) and excited-state OD ($^2\Sigma$) accompany the D^- anions produced within the third resonance peak, and that the three-body breakup channel D^-+D+O is observed toward the high-energy tail of the second peak.

All the experimental studies determined that there are three metastable electronic resonance states of the H_2O^- anion, the $^2B_1$, $^2A_1$, and $^2B_2$, which are primarily responsible for dissociative electron attachment to water. These three electronic states correspond to the three peaks seen in the experimental cross sections. Although the third peak is not obvious in the H^- cross sections, it is present, though much smaller than the first and second peaks.

Several salient features of the early experiments suggest that the nuclear dynamics of this process may hold some surprises. For dissociative attachment through the $^2B_1$ resonance, the cross section for producing H^-+OH is roughly 40 times larger at its peak than the cross section for producing the energetically favored products, O^-+H_2 [5,6]. The lowest-energy atom-diatom arrangement, $H+OH^-$, is produced in even smaller quantities. In addition, the branching ratios for the different product states vary greatly depending on which Feshbach resonance is formed by the attachment. These observations indicate that the products of this reaction are determined by the dynamics of the process itself rather than by the energetics of the possible product channels, and that moreover those dynamics are different for each of the resonance states of the water anion. The detailed experiments of Belić, Landau, and Hall [9] in 1981 indicated that the dissociation dynamics involve correlated motion among multiple degrees of freedom. For instance, the channel producing H^-+OH through the $^2B_1$ resonance state is accompanied by extensive vibrational excitation of the OH fragment.

Therefore, given the competition between dissociation channels and the observed product vibrational excitation, one expects that the dynamics of dissociative attachment to this molecule are intrinsically polyatomic, and can only be described theoretically by a treatment using the full dimensionality of nuclear motion.

Compared with the large number of experimental measurements, detailed theoretical work on dissociative electron-water collisions has been relatively scarce. The paucity of theoretical work on DA stems from the fact that, in water, DA proceeds not through tunneling shape resonances, but through Feshbach resonances that involve changes in the electronic structure of the target. Early theoretical work focused on the electronic structure [11] and configuration-interaction [12] calculations on various states of H_2O^- that are possible resonances. These calculations, together with experimental observations, formed the basis of the assignment of the three Feshbach resonances that are responsible for electron-impact dissociation of water in the gas phase.

Contemporary theoretical work has included *ab initio* complex Kohn [13] and *R*-matrix [14] calculations, at the equilibrium nuclear geometry, of the resonances and excitation cross sections into low-lying dissociative electronic states. More recently, Gorfinkiel, Morgan, and Tennyson [15] carried out *R*-matrix calculations of dissociative excitation of water through the four lowest excited states (the $^{1,3}B_1$ and $^{3,1}A_1$ states). A limited study of the effects of nuclear motion was included in that work by increasing one of the OH bonds while keeping the equilibrium H-O-H bond angle and the other OH bond length constant. The only theoretical work on the dynamical aspects of dissociative electron attachment to water is earlier classical trajectory analyses based on either repulsive [27] or attractive [28] model resonance surfaces.

We previously reported calculations of the cross sections for dissociative attachment through the lowest-energy $^2B_1$ resonance [16,17] that incorporated a full quantum treatment of the nuclear motion of the resonant state. That study found good agreement with experiment for dissociative attachment through the lowest resonance state ($^2B_1$) of the water anion to produce H^-, and it established that the associated dynamics are intrinsically polyatomic and thus cannot be described successfully by one-dimensional models. The present treatment supersedes our earlier study and extends the treatment to include the higher resonance states as well.

We have recently presented a qualitative study [18] of the potential-energy surfaces for the three Feshbach resonances, which demonstrated that for these metastable, anion states, there exist numerous intersections and degeneracies within the adiabatic manifold. This study identified the conical intersection between the $^2A_1$ and $^2B_2$ states, as well as a novel degeneracy between the $^2B_2$ Feshbach resonance and a $^2B_2$ shape resonance. This degeneracy defines a branch seam, and

the two resonance energies are seen to comprise two components of a double-valued adiabatic potential-energy surface. This seam and the resulting dynamics may have an effect on the three-body, $H+H+O^-$ cross section, although we do not include it in the present treatment. Finally, in a separate publication [19], we derived a "constant-eigenmode approximation" and used it to calculate the angular dependence of the H^- fragment production [19] via the $^2B_1$ resonance. We found excellent agreement with the results of Belic, Landau, and Hall [9], and demonstrated that the observed angular dependence is a result of partial-wave mixing in the resonance-background coupling.

III. LOCAL COMPLEX POTENTIAL MODEL

We treat the nuclear dynamics of dissociative electron attachment within the local complex potential model. This model is concerned with the proper accounting for the decay of the resonant state, and its effect upon the nuclear dynamics. The LCP model includes the simplest such accounting, in which the decay rate is a local function of the nuclear geometry.

A. Feshbach partitioning and the nuclear wave equation

The local complex potential model [21–23], also known as the "Boomerang" model when applied to vibrational excitation, describes resonance nuclear motion by an inhomogeneous Schrödinger equation and a complex, but purely local potential. It is perhaps easiest to derive by applying Feshbach partitioning [29] within the Born-Oppenheimer framework to derive a nuclear wave equation [24,25]. The derivation begins by defining a discrete (square-integrable) approximation to the resonant electronic state, $\psi_Q(\vec{r}_e;\vec{q})$, which depends parametrically on the nuclear coordinates $\vec{q}$ and which is unit-normalized with respect to integration over the electronic coordinates $\vec{r}_e$. One then defines the geometry-dependent Feshbach projection operator Q, which operates on the electronic degrees of freedom,

$$Q(\vec{q}) = |\psi_Q(\vec{q})][\psi_Q(\vec{q})|, \tag{2}$$

and its complement P,

$$P(\vec{q}) = \mathbf{1} - Q(\vec{q}), \tag{3}$$

with $P^2=P$, $Q^2=Q$, and $PQ=QP=0$. (Brackets denote integration over the electronic degrees of freedom only.) Partitioning the full wave function for total energy E as $\Psi^+ = P\Psi^+ + Q\Psi^+$, we can formally derive the following inhomogenous equation for $Q\Psi^+$:

$$\left(E - Q\mathbf{H}Q - Q\mathbf{H}P\frac{1}{E - P\mathbf{H}P + i\epsilon}P\mathbf{H}Q\right)Q\Psi^+ = Q\mathbf{H}P\Psi^+, \tag{4}$$

where H is the sum of the electronic Hamiltonian and nuclear kinetic energy, $\mathbf{H}=H_{\rm el}+T_{\vec{q}}$.

In view of Eq. (2), we can write

$$Q\Psi^+(\vec{r}_e;\vec{q}) = \psi_Q(\vec{r}_e;\vec{q})\xi(\vec{q}). \tag{5}$$

The function $\xi(\vec{q})$ describes the relative motion of the nuclei in the negative-ion resonance state. To derive an equation for $\xi(\vec{q})$, the first approximation that is made is the Born-Oppenheimer approximation: we neglect all nonadiabatic couplings arising from the operation of the nuclear kinetic energy upon the adiabatic basis. Then multiplying Eq. (4) from the left by $\psi_Q(\vec{r}_e;\vec{q})$ and integrating oven the electronic coordinates gives the nuclear wave equation,

$$[E - V_Q(\vec{q}) - \Delta(E) - T_{\vec{q}}]\xi(\vec{q}) = QH_{\rm el}P\Psi^+, \tag{6}$$

where

$$V_Q(\vec{q}) \equiv [\psi_Q|H_{\rm el}|\psi_Q] \tag{7a}$$

and

$$\Delta(E) \equiv QH_{\rm el}P\frac{1}{E - PH_{\rm el}P - T_{\vec{q}} + i\epsilon}PH_{\rm el}Q. \tag{7b}$$

The real-valued potential $V_Q(\vec{q})$ is the expectation value of the electronic Hamiltonian with respect to the discrete state ψ_Q; the additional, energy-dependent term $\Delta(E)$ is called the "level-shift operator" and is nonlocal in the nuclear degrees of freedom $\vec{q}$, owing to the presence of the nuclear Green's function. The residue of this Green's function gives the level-shift operator $\Delta(E)$ a negative-definite imaginary component.

In order to bring Eq. (6) into the form of the local complex potential model, it is necessary to make a local approximation to the level-shift operator $\Delta(E)$, and also to approximate the driving term. The assumptions that underlie these approximations are well understood [30,31]. A local approximation to the level-shift operator yields

$$V_Q(\vec{q}) + \Delta(E) \approx E_R(\vec{q}) - i\frac{\Gamma(\vec{q})}{2}, \tag{8}$$

where E_R and Γ are the location and *total* width of the resonance. A first-order perturbation treatment (Fermi's golden rule) of the driving term yields [19]

$$QH_{\rm el}P\Psi^+ \approx \sqrt{\frac{\Gamma_0(\vec{q})}{2\pi}}\chi_{\nu_i}(\vec{q}) \equiv \phi_{\nu_i}(\vec{q},0), \tag{9}$$

where Γ_0 is the *partial* width for decay to the ground electronic state of the target, and χ_{ν_i} is the initial rovibrational state of the target.

The final working equation of the LCP model then reads

$$\left(E - E_R(\vec{q}) + \frac{i\Gamma(\vec{q})}{2} - T_{\vec{q}}\right)\xi_{\nu_i}(\vec{q}) = \sqrt{\frac{\Gamma_0(\vec{q})}{2\pi}}\chi_{\nu_i}(\vec{q}). \tag{10}$$

The location and widths of the various resonance states were obtained from configuration interaction and fixed-nuclei variational electron scattering calculations, respectively, as detailed in paper I. In the case of the $^2B_1$ resonance, which generally lies below its $^3B_1$ neutral parent, the resonance can only decay into the ground electronic channel. In that case, the total and partial widths, Γ and Γ_0, coincide and can be obtained by fitting the eigenphase sum to a Breit-Wigner

form. For the higher resonances, a more elaborate fitting procedure is required to obtain the partial widths, as outlined in Ref. [19] and in paper I.

B. Time-dependent formulation of the LCP model

A direct solution of the differential equations of the local complex potential model can pose significant difficulties for problems with multiple degrees of freedom, and, in such cases, a time-dependent formulation of the problem can offer distinct computational advantages. Such a formulation can be made, as demonstrated by McCurdy and Turner [32], by formally writing the solution of Eq. (10) as

$$\xi_{\nu_i}(\vec{q}) = (E - H + i\epsilon)^{-1}\phi_{\nu_i}(\vec{q},0) \tag{11}$$

and writing the nuclear Green's function as the Fourier transform of the propagator for the time-dependent Schrödinger equation,

$$\xi_{\nu_i}(\vec{q}) = \lim_{\epsilon\to 0} i\int_0^\infty e^{i(E+i\epsilon)t}e^{-iHt}\phi_{\nu_i}(\vec{q},0)dt$$

$$= \lim_{\epsilon\to 0} i\int_0^\infty e^{i(E+i\epsilon)t}\phi_{\nu_i}(\vec{q},t)dt, \tag{12}$$

where we define the time-dependent nuclear wave function as

$$\phi_{\nu_i}(\vec{q},t) = e^{-iHt}\phi_{\nu_i}(\vec{q},0). \tag{13}$$

The driving term $\phi_{\nu_i}(\vec{q},0)$ of the LCP equation can thus be viewed as the initial value of a wave packet that subsequently evolves on the complex potential surface of the resonance anion. Since the potential surface is complex, the packet decays as a function of time until it effectively escapes the region of the surface where the width is nonzero.

IV. TRIATOMIC JACOBI COORDINATE SYSTEM AND HAMILTONIAN

The LCP model equations were solved in the coordinate systems depicted in Fig. 2. For the three internal degrees of freedom of this triatomic molecule, we employ Jacobi coordinate systems, which are depicted at the top of this figure. The Jacobi coordinate system on the left, marked "(a)," is used to analyze the OH+H arrangement; the one on the right, marked "(b)," is used for the H_2+O arrangement. The vector $\vec{r}$ connects the nuclei of the diatomic. The vector $\vec{R}$ connects the center of mass of the diatomic to the third atom. R is the length of $\vec{R}$, r is the length of $\vec{r}$, and γ is the angle between the $\vec{R}$ and $\vec{r}$ vectors. For (a), γ=0 denotes a linear OHH configuration.

In addition to the three internal degrees of freedom, there are also the three Euler angles that orient the internal or body-fixed (BF) frame with respect to the lab or space-fixed (SF) frame. The origin of both frames is the center of mass. The space-fixed Z axis is always chosen to be parallel with the wave vector of the incident electron. For calculations with total rotational angular momentum J=0, the Hamiltonian only operates on the internal degrees of freedom. For $J \neq 0$ we must take the Euler angles into account, and we denote them by α, β, ζ.

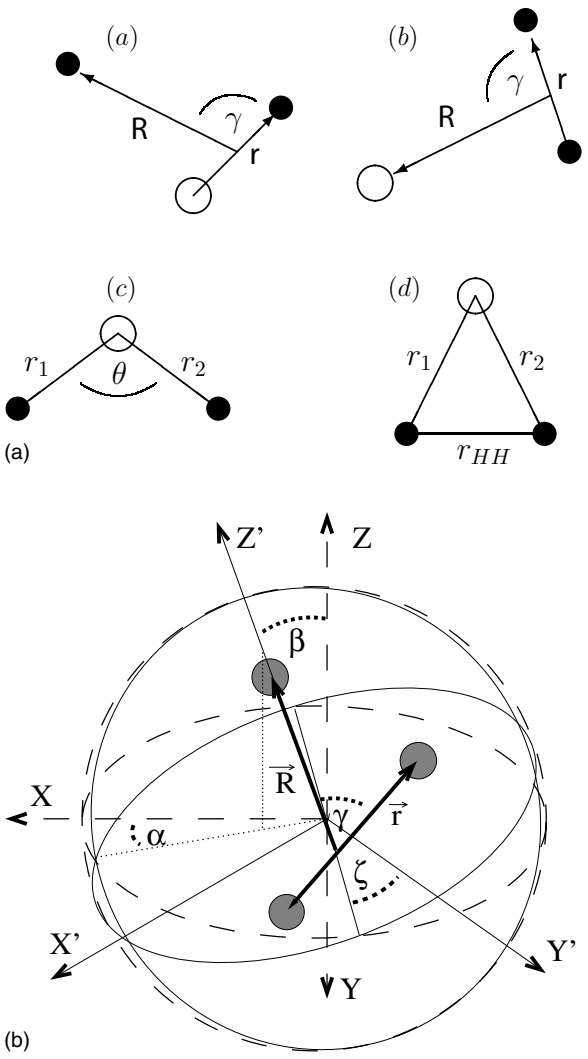

FIG. 2. Jacobi coordinate systems used to analyze the OH+H (a) and H_2+O (b) arrangement channels and the "R-embedding" coordinate system with origin at the center of mass. Primed and unprimed axes refer to BF and SF frames, respectively. The BF $X'Z'$ and $X'Y'$ planes are both marked with a thin line circle and the SF XZ and XY planes are marked with dashed circles. The line of nodes is also drawn. The molecule resides in the BF $X'Z'$ plane.

The total (electronic plus nuclear, ignoring spin) angular momentum, J, and its projection upon the space-fixed Z axis, M, are quantum numbers conserved by the Hamiltonian. We also use the quantum number K to specify the projection of the angular momentum on a BF axis. K is not a conserved quantity and there is some flexibility in its definition. We use the "R-embedding" scheme [33] in which $\vec{R}$ is taken to be collinear with the BF Z' axis and the angular momentum number K is quantized around this axis. With this convention, the Euler angles α and β are the polar angles which orient the R vector with respect to the SF frame, and ζ is the third Euler angle specifying orientation about the BF Z' axis. A schematic of the coordinate system is also shown in Fig. 2.

We may write a general expression for the six-dimensional rovibrational wave function for a triatomic with specified J and M value as follows:

$$\chi_{\nu_i}(R,r,\gamma,\alpha,\beta,\zeta) = \sum_K \widetilde{D}^J_{MK}(\alpha,\beta,\zeta)\frac{\chi^K_{\nu_i}(R,r,\gamma)}{Rr}, \quad (14)$$

where the basis of $\widetilde{D}^J_{MK}(\alpha,\beta,\zeta)$ is the set of normalized Wigner rotation matrices (and BF angular momentum eigenstates),

$$\widetilde{D}^J_{MK}(\alpha,\beta,\zeta) = \sqrt{\frac{2J+1}{8\pi^2}}D^J_{MK}(\alpha,\beta,\zeta) \quad (15)$$

such that

$$\int_0^{2\pi} d\alpha \int_{-1}^{1} d(\cos\beta) \int_0^{2\pi} d\zeta \times \widetilde{D}^J_{MK}(\alpha,\beta,\zeta)\widetilde{D}^{J'*}_{M'K'}(\alpha,\beta,\zeta) = \delta_{J,J'}\delta_{M,M'}\delta_{K,K'}. \quad (16)$$

In Eqs. (15) and (16), we follow the conventions of Zhang [34], which for the D^J_{MK} is the same as that of Edmonds [35].

The standard [36,37] BF Hamiltonian for the radial solutions $\chi^K_{\nu_i}$ of this expansion incorporates coupling among the different K values for a given total angular momentum J. The neglect of this coupling is termed the "coupled states" or "centrifugal sudden" (CS) approximation [38,39], and we employ this approximation for our calculations, since the kinetic energies of the recoiling fragments are large compared to their centrifugal energies. The resulting Hamiltonian is thus diagonal in K and can be written

$$H^J_K = \frac{-1}{2\mu_R}\frac{\partial^2}{\partial R^2} + \frac{-1}{2\mu_r}\frac{\partial^2}{\partial r^2} + \left(\frac{\hat{j}^2}{2\mu_r r^2} + \frac{\hat{j}^2}{2\mu_R R^2}\right) + \frac{J(J+1)-2K^2}{2\mu_R R^2} + V(R,r,\gamma),$$

$$\hat{j}^2 = -\left(\frac{1}{\sin\gamma}\frac{\partial}{\partial\gamma}\sin\gamma\frac{\partial}{\partial\gamma} - \frac{K^2}{\sin^2\gamma}\right), \quad (17)$$

where μ_r and μ_R are the reduced masses in either degree of freedom and V is the (coupled set of) Born-Oppenheimer potential-energy surface(s) that we calculate.

A. Inclusion of Renner-Teller coupling

For dynamics beginning on the $^2A_1$ ($1\,^2A'$) resonance surface, the gradient of that surface will force the wave packet toward linear geometry, at which point this resonance state is degenerate with the $^2B_1$ resonance (see Fig. 1). The Renner-Teller effect [36,40–46] will therefore couple these two components of the $^2\Pi$ state, and we modify the Hamiltonian of Eq. (17) accordingly.

The quantum numbers $J(J+1)$ and K in Eq. (17) are obtained as eigenvalues of the total angular momentum operators $\hat{J}^2$ and $\hat{J}'_z$,

$$\hat{J}'_z\left(\widetilde{D}^J_{MK}(\alpha,\beta,\zeta)\frac{\chi^K_{\nu_i}(R,r,\gamma)}{Rr}\right) = K\left(\widetilde{D}^J_{MK}(\alpha,\beta,\zeta)\frac{\chi^K_{\nu_i}(R,r,\gamma)}{Rr}\right), \quad (18)$$

etc., where $\hat{J}'_z$ has a simple form in terms of derivative operators in (α,β,ζ) [47]. Properly, the operators that appear in the Born-Oppenheimer Hamiltonian for the rovibrational motion of the nuclei, Eq. (17), should be not $\hat{J}^2$ and $\hat{J}'_z$ but the *nuclear* angular momentum operators $\hat{R}^2$ and $\hat{R}_z$, where

$$\hat{R}_i = \hat{J}_i - \hat{l}_i, \quad (19)$$

in which expression $\hat{l}_i$ is an electronic angular momentum operator; the Hamiltonian [36] with this form is exact except for the omission of the mass-polarization term.

The exact Hamiltonian [36] introduces numerous new diagonal and off-diagonal (off-diagonal in K, electronic state, and both) coupling terms to the triatomic Hamiltonian. The term that is most commonly labeled the Renner-Teller coupling comes from the $\hat{j}^2$ term in Eq. (17)

$$\left(\frac{1}{2\mu_r r^2} + \frac{1}{2\mu_R R^2}\right)\frac{K^2}{\sin^2\gamma} \rightarrow \left(\frac{1}{2\mu_r r^2} + \frac{1}{2\mu_R R^2}\right)\frac{\hat{R}^2_z}{\sin^2\gamma} = \left(\frac{1}{2\mu_r r^2} + \frac{1}{2\mu_R R^2}\right)\frac{K^2 - 2K\hat{l}_z + \hat{l}^2_z}{\sin^2\gamma}. \quad (20)$$

It is the $2K\hat{l}_z$ term that couples the two components (sine and cosine, $^2B_1$ and $1\,^2A'$) of the $^2\Pi$ state at linear geometry. At such geometries the operator $\hat{l}_z$ is diagonalized by

$$\hat{l}_z(\psi_{A'} \pm i\psi_{B1}) = \pm 1 \times (\psi_{A'} \pm i\psi_{B1}) \quad (21)$$

The matrix elements of l_z may either be computed [41,45,46] or approximated by their values at linear geometry [42,43]. We take the latter route, i.e., we assume that Eq. (21) holds everywhere. This approximation has little effect on the dynamics because only near linear geometry does the coupling become large. We perform our Renner-Teller calculations in the $(l_z=\pm 1)$ diabatic basis because it allows us to incorporate the boundary condition in γ using the "K-Legendre" discrete variable representation [37]. With this assumption, for a given value of K, the $(l_z=\pm 1)$ diabatic states have $R_z=K\pm 1$. The kinetic energy operator in Eq. (20) is diagonal in this diabatic basis. The coupling then arises from the electronic Hamiltonian, which is not diagonal in this basis. The electronic Hamiltonian in this basis takes the form

$$V = \frac{1}{2}\begin{pmatrix} V_{A'} + V_{B_1} & V_{A'} - V_{B_1} \\ V_{A'} - V_{B_1} & V_{A'} + V_{B_1} \end{pmatrix}, \quad (22)$$

i.e., the diabatic states are degenerate. When $K=0$, there is no Renner-Teller effect, since the coupling term in Eq. (20) vanishes.

V. THE MULTICONFIGURATION TIME-DEPENDENT HARTREE METHOD

The multiconfiguration time-dependent Hartree or MCTDH [48–51] method is an efficient adaptive scheme for propagating quantum-mechanical wave packets for systems with multiple degrees of freedom. We use this method to perform the propagation in Eq. (13). We use the implementation within the MCTDH package [52], a freely available suite of codes built at the University of Heidelberg, Germany.

In the MCTDH method, as in other methods developed for solving the time-dependent Schrödinger equation, we start with a time-independent orthonormal product basis set,

$$\{\chi_{j_1}^{(1)}(q_1), \ldots, \chi_{j_f}^{(f)}(q_f)\}, \quad j_\kappa = 1, \ldots, N_\kappa \tag{23}$$

for a problem with f degrees of freedom and nuclear coordinates labeled $q_1, \ldots, q_f$. For computational efficiency, the basis functions $\chi_{j_\kappa}^{(\kappa)}$ are chosen as the basis functions of a discrete variable representation (DVR) [53].

The central idea of the MCTDH technique is the representation of the nuclear wave packet as a sum of separable terms,

$$\phi_{\nu_i}(\vec{q},t) = \sum_{j_1=1}^{n_1} \cdots \sum_{j_f=1}^{n_f} A_{j_1,\ldots,j_f}(t) \prod_{\kappa=1}^{f} \varphi_{j_\kappa}^{(\kappa)}(q_\kappa,t), \tag{24}$$

with $n_\kappa \ll N_\kappa$. Each "single-particle function" (or SPF) $\varphi_{j_\kappa}^{(\kappa)}(q_\kappa,t)$ is itself represented in terms of the primitive basis,

$$\varphi_{j_\kappa}^{(\kappa)}(q_\kappa,t) = \sum_{i_\kappa=1}^{N_\kappa} c_{i_\kappa j_\kappa}^{(\kappa)}(t) \chi_{i_\kappa}^{(\kappa)}(q_\kappa). \tag{25}$$

One can derive equations of motion for the parameters $c_{i_\kappa j_\kappa}^{(\kappa)}(t)$ and $A_{j_1,\ldots,j_f}(t)$. Since both the coefficients $A_{j_1,\ldots,j_f}$ and the single-particle functions $\varphi_{j_\kappa}^{(\kappa)}$ are time-dependent, the wave-function representation is made unique by imposing additional constraints on the single-particle functions, which keep them orthonormal for all times [50].

The evaluation of the Hamiltonian matrix, which must be carried out at every time step, is expedited [49,50] if the Hamiltonian can be written as a sum of products of single-coordinate operators. The MCTDH package [52] includes a utility that performs a fit of a given potential to a separable representation of this form. Details can be found in Beck *et al.* [50]. All potential-energy surfaces used in the current calculation were represented in this manner, using this utility to fit them specifically for each choice of the DVR grids.

For calculations on the electronically coupled $^2A_1$ and $^2B_2$ states, the underlying DVR is the same for each electronic state, but each electronic state has its own set of single-particle functions $\varphi_{j_\kappa}^{(\kappa)}$. This is referred to as the "multiset" formalism, as opposed to "single-set." The Renner-Teller coupled $1\,^2A' - ^2B_1$ calculation is performed under the single-set formalism.

A. Complex absorbing potentials

The sine DVR bases in the r and R degrees of freedom incorporate standing-wave boundary conditions at their edges. Therefore, when the dissociating wave packet reaches the end of the DVR grid, it must be absorbed to prevent unphysical reflections. To this end we include an artificial negative imaginary component to the surface called a "complex absorbing potential" or CAP [54,55],

$$V_{\mathrm{CAP}} = \begin{cases} 0 & (R \le R_c) \\ i\eta(R - R_c)^2 & (R \ge R_c); \end{cases} \tag{26}$$

a similar expression for the CAP in the r degree of freedom also applies. Formally, the CAP's provide the $+i\epsilon$ limit in Eq. (12).

We use a value for η equal to 0.007 hartree, and place R_c three bohr before the end of our grid, except for the $1\,^2A'$ calculations for H_2 and D_2, for which we use a strength of 0.0018 hartree and a value of R_c five bohr before the end of the grid.

B. Dissociative attachment cross sections from outgoing projected flux

The cross sections for dissociative attachment can be calculated directly from the time-propagated wave packet by computing the energy-resolved, outgoing projected flux. The energy resolution is achieved by Fourier transform and a final-state resolution is achieved by the introduction of appropriate projection operators. For DEA to a specific final rovibrational state labeled by rotational (j) and vibrational (ν) indices, we use the projection operator

$$P_{j\nu} = \left| \frac{\chi_{j\nu}}{r} \right\rangle \left\langle \frac{\chi_{j\nu}}{r} \right|. \tag{27}$$

The flux operator, which measures the flux passing through a surface defined by $R = R_c$, is defined as

$$\hat{F} = i[H, h(R - R_c)], \tag{28}$$

where h is a Heaviside function. The energy-resolved projected flux is then given by

$$F_{j\nu}(E) = \frac{1}{2\pi} \int_0^\infty dt \int_0^\infty dt' \times \langle \phi_{\nu_i} | e^{i(H-E)t} P_{j\nu} \hat{F} P_{j\nu} e^{-i(H-E)t'} | \phi_{\nu_i} \rangle. \tag{29}$$

The MCTDH package [52] includes a utility that computes the outgoing projected flux. In the actual calculations, the flux operator appearing in the equation above is replaced by an expression involving the complex absorbing potential, Eq. (26). This formulation of the flux operator is very convenient numerically and entirely equivalent to the traditional formal definition of the operator in this context, in the limit that the CAP does not perturb the propagating wave packet beyond first order, which in the present case, given the nuclear masses, holds as a good approximation. For more details on this CAP flux formalism, see Refs. [50,51,56].

The resulting energy-resolved projected flux is that associated with the time-independent solution of the driven

Schrödinger equation of the LCP model in Eq. (10),

$$F_{j\nu}(E) = \frac{1}{2\pi}\langle \xi_{\nu_i}|P_{j\nu}\hat{F}P_{j\nu}|\xi_{\nu_i}\rangle. \tag{30}$$

In terms of $F_{j\nu}$, the DEA cross section is [17]

$$\sigma_{\mathrm{DEA}}^{j\nu} = \frac{4\pi^3}{k^2}F_{j\nu}\left(E_{\nu_i} + \frac{k^2}{2}\right). \tag{31}$$

For the $H^- + OH$ channel, an additional factor of 2 is included in Eq. (31) to account for the fact that in a given calculation we perform the flux analysis for only one of the two $H^- + OH$ arrangements, namely the one for which the Jacobi coordinates are appropriate.

The definition of the rovibrational states $\chi_{j\nu}$ is complicated by the ion-dipole interaction of the fragments. In our earlier study DEA to water via the $^2B_1$ Feshbach resonance [17], we attempted a complete final-state analysis, and projected on pendular (restricted rotor) states [57], not free rotational states, and assumed that these pendular states evolve adiabatically to their free rotational state asymptotes. This analysis did not yield any major insight, and so for the present calculations we simply project on free rotational states. As a consequence, there is a small error in our final-state resolution, but the magnitude of this error will span a range of states and a range of energies approximately equal to the magnitude of the ion-dipole interaction at the edge of our grid, which is small compared to the kinetic energy spread of the fragments.

C. The DVR bases and other MCTDH parameters

In most of the calculations reported here, we used DVR primitive basis sets for all internal degrees of freedom, choosing the standard sine DVR [50] for the r and R degrees of freedom and, for $J=0$, the Legendre DVR [50] for γ. For $J>0$, as previously discussed, the DVR for γ must be modified to account for singularities in the Hamiltonian [see Eq. (17)] due to the term $K^2/\sin^2(\gamma)$. This is done by using an extended Legendre DVR [37,58,59], which is implemented in the Heidelberg MCTDH package [52].

D. Initial states

The initial rovibrational states χ_{ν_i} of Eq. (9) were obtained via relaxation and improved relaxation [51] as implemented within the MCTDH package [52]. In relaxation runs, an initial guess $\chi_g(\vec{q},0)$ for the ground state is propagated in imaginary time, which yields the ground state $\chi_0(\vec{q})$,

$$\chi_g(\vec{q},\tau) = e^{-H\tau}\chi_g(\vec{q},0) \underset{\tau\to\infty}{\longrightarrow} \chi_0(\vec{q}). \tag{32}$$

In improved relaxation runs, the propagation of the SPF expansion coefficients $c_{i_\kappa j_\kappa}^{(\kappa)}(\tau)$ of Eq. (25) is performed via Eq. (32), but the configuration coefficients $A_{j_1,\ldots,j_f}(t)$ are obtained anew at each time step via a Davidson diagonalization.

For the two-state $^2B_2$–$^2A_1$ calculations, the wave function is represented in the diabatic basis, each component of which has an expansion of the form of Eq. (24), and different sets of time-dependent single-particle functions $\varphi_{j_\kappa}^{(\kappa)}(q_\kappa,t)$. Since the adiabatic-to-diabatic transformation angle is not constant with geometry, the single-particle functions that represent the initial state will be different in the diabatic basis than in the adiabatic basis (in which they would be identical to the single-particle functions of the relaxation run). For this reason, an iterative technique [50] is employed to minimize the error between the diabatic representation and its adiabatic representation.

VI. CALCULATED CROSS SECTIONS FOR DISSOCIATIVE ELECTRON ATTACHMENT TO WATER

We will present cross sections for dissociative electron attachment to water into the three different atom-diatom arrangements, which are present as asymptotes of the $^2B_1$, $^2A_1$, and $^2B_2$ Feshbach resonances,

$$H_2O + e^- \rightarrow \begin{cases} H_2 + O^- & 3.56\ \mathrm{eV} \\ H^- + OH\ (X^2\Pi) & 4.35\ \mathrm{eV} \\ H^- + OH^*\ (^2\Sigma) & 8.38\ \mathrm{eV}, \end{cases}$$

resolved into the final rovibrational states of the diatomic fragment, as a function of incident electron energy. The final-state resolution allows us to determine the kinetic energy of the diatomic fragment. Therefore, we are able to calculate cross sections as a function of both the incident electron energy and the kinetic energy of the recoil, which data we may easily compare with experiment. These two-dimensional data provide a comprehensive view of dissociative attachment via each of the resonances. We calculate the degree of rotational and vibrational excitation, and show how these quantities change with the incident electron energies.

We have obtained converged cross sections for all channels considered, with two exceptions. For the Renner-Teller coupled $^2A_1$ ($1^2A'$)-$^2B_1$ states, we have been unable to obtain a nonzero result for the minor H_2+O^- channel, as well as its deuterated counterpart. For the production of H^- from the $^2B_2$ state, coupled to the $^2A_1$ state via the conical intersection, our calculations are not fully converged, although we do obtain total cross sections and, for the OH ($^2\Sigma$) fragment, final-state resolution.

In general, our results are in qualitative, though not quantitative, agreement with the experimentally measured cross sections for the *major* product arrangements observed in DEA via each resonance state: H^-+OH from the $^2B_1$ and $^2A_1$ resonances and H_2+O^- from the highest-energy $^2B_2$ resonance. We have had difficulty obtaining results for the minor channels, failing to reproduce the experimental result for the magnitude of the cross section for production of H_2+O^- via the first two resonances and not being able to fully converge the calculation for production of H^-+OH ($^2\Pi$ or $^2\Sigma$) via the $^2B_2$ resonance.

Total cross sections calculated for the two anion-diatom arrangements, and for both D_2O and H_2O, are presented in Fig. 3, along with recent experimental results from Fedor *et al.* [20]. Calculated and experimental peak heights and locations are collected in Table I. In Fig. 3, the experimental data

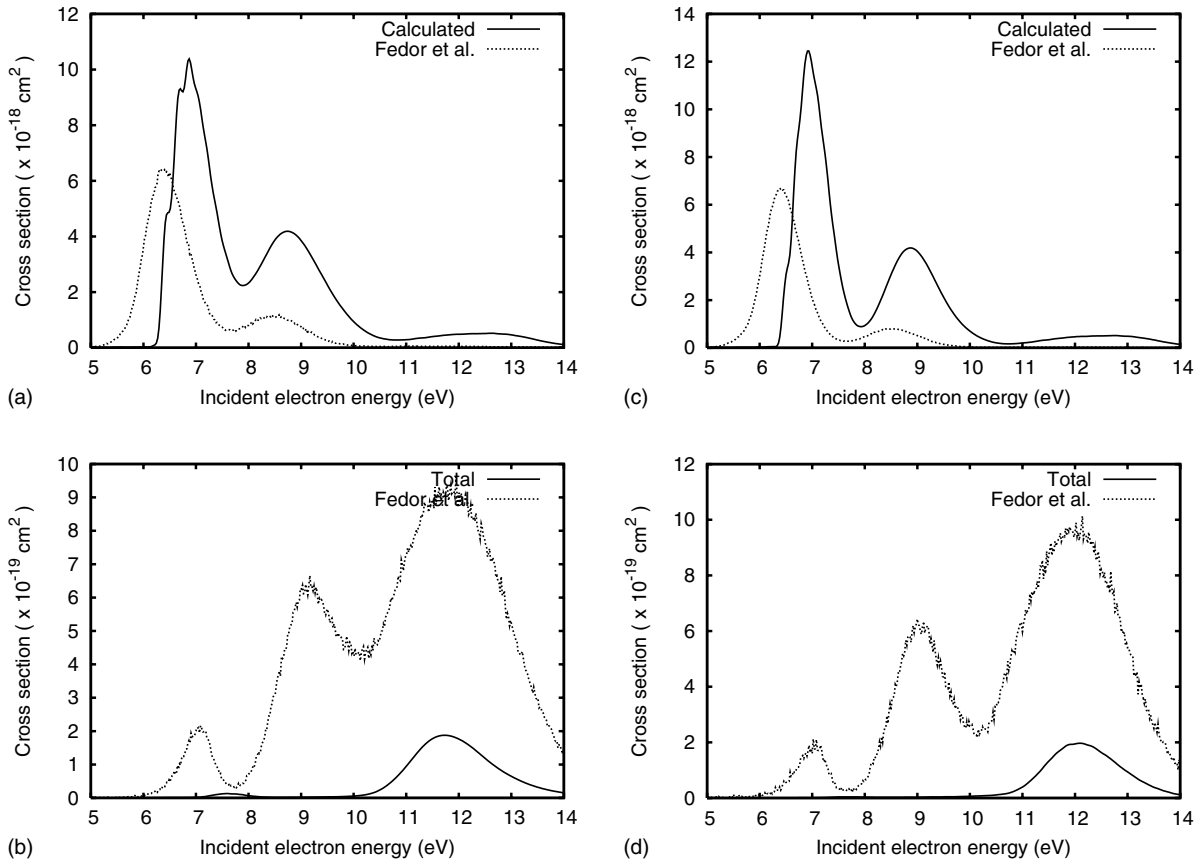

FIG. 3. Cross sections for production of H^--D^- (left) and O^- (right) as a function of incident electron energy, summed from different MCTDH calculations. Top, cross sections from H_2O; bottom, cross sections from D_2O. Experimental results of Fedor *et al.* [20] included for comparison. The experimental data, which do not have absolute normalization, are normalized to agree with Compton and Christophoreau's [5] H^-+OH peak height for DEA via the $^2B_1$ resonance at 6.5×10^{-18} cm^2.

are internormalized but not absolutely normalized; therefore, for the purposes of comparison, we normalize the experimental peak for the production of H^-+OH via the lowest-energy $^2B_1$ resonance to Compton and Christophoreau's [5] result of 6.5×10^{-19} cm^2. The calculated curves are obtained by summing the cross sections into the individual rovibrational states $\chi_{j\nu}$ of the ion + diatom arrangement. Therefore, the three-body cross sections are neglected. The recent experimental results of Ref. [20] do not resolve the kinetic energy of the atom-diatom recoil and therefore do not distinguish between the two- and three-body DEA cross section. Thus, to the degree that three-body breakup is important, our calculated results cannot be compared directly with these experiments for incident electron energies that exceed the three-body dissociative thresholds of either 8.04 eV (H+H+O^-)or 8.75 eV (H+H^-+O).

We can draw the following conclusions from Fig. 3 and Table I. First, it is clear that the entrance amplitude for the $^2B_1$ resonance has been overestimated by our present study, because the magnitude of the DEA cross section via this resonance is entirely controlled by its entrance amplitude, and we have overestimated the experimental peak height by nearly 60%. Also, similar to the result of our previous study [16,17], we overestimate the energy at which the H^- cross section via the $^2B_1$ state peaks by about 0.4 eV. The calculated peak location, 6.87 eV, is larger than the vertical transition energy for the $^2B_1$ resonance as defined by our potential-energy surface constructed in paper I, which is 6.63 eV. This value is obtained through a configuration-interaction treatment of the resonance; using complex Kohn scattering calculations, we obtained a value of 6.09 eV. The comparison between the calculated and experimental peak locations indicates that the physical value of the vertical transition energy for the $^2B_1$ Feshbach resonance is probably about 6.2 eV, nearer to the complex Kohn result.

Similar observations apply to the comparison between the calculated and experimental results for DEA via the $^2A_1$ resonance to produce H^-+OH; the calculated peak height is too large and located at a higher energy than is experimentally observed. Therefore, it is possible that we have overestimated the entrance amplitude and the vertical transition energy for this resonance as well. The transition energy as defined by our potential-energy surface is 9.01 eV; from complex Kohn calculations we obtained a lower result of 8.41 eV, which is probably closer to the physical value. However, as we explain further below, the disagreement in magnitude and location between the calculated and observed results may indicate a breakdown of the local complex model for DEA via the $^2A_1$ resonance.

The data in Fig. 3 and Table I indicate that, while the calculations overestimate the cross sections for H^-+OH production, they evidently underestimate those for H_2+O^- pro-

TABLE I. Peak cross sections (σ, in units of 10^{-19} cm^2) and peak locations (E, in eV) calculated for DEA via the three resonances. Experimental peak locations are taken from the data of Fedor *et al.*, except where noted.

		Calculated			Experiment		
	$^2B_1$	$^2A_1$	$^2B_2$	$^2B_1$	$^2A_1$	$^2B_2$	
$OH+H^-$	σ	103.7	41.4	2.61[a]	65[b]	13[b]	
($X^2\Pi$)	E	6.87	8.74	11.54	6.4	8.4	
$OH+H^-$	σ			3.67[a]			
($^2\Sigma$)	E			12.68			
H^-	σ			5.21[a]			?
(total, $^2B_2$)	E			12.61			11.8[c]
H_2+O^-	σ	0.121	**0**	1.87	1.3[d]	3.2[d]	5.7[d]
	E	7.62		11.75	7.1	9.0	11.8
$OD+D^-$	σ	124.4	41.6	1.45[a]	52[b]	6[b]	
($X^2\Pi$)	E	6.93	8.87	11.93	6.4	8.5	
$OD + D^-$	σ			1.96[a]			
($^2\Sigma$)	E			12.86			
D^-	σ			2.60[a]			?
(total, $^2B_2$)	E			12.57			
D_2+O^-	σ	0.0242	**0**	1.97	?	?	?
	E	7.63		12.10	7.1	9.0	12.0

[a]Calculation not converged for H^-+OH arrangement via $^2B_2$ resonance.
[b]Compton and Christophoreau, Ref. [5].
[c]Jungen, Ref. [12].
[d]Melton, Ref. [6].

duction. H_2+O^- is the major channel for DEA via the $^2B_2$ resonance. As explained in Ref. [18], the presence of this channel is entirely due to nonadiabatic coupling between the upper $^2B_2$ ($2^2A'$) resonance and the lower $^2A_1$ ($1^2A'$) resonance via their conical intersection. As we will show, the magnitude of this cross section is determined by active competition between different product arrangements, the dynamic effects of both the real and imaginary components of the surface, as well as the conical intersection dynamics. We regard the agreement with experiment that we have obtained to be quite good, considering the complexity of the system. We note that the location of the calculated peak for O^- production which we have calculated(11.75 eV) agrees well with the experimental value (11.8 eV). The peak location may be contrasted with the vertical excitation energy, which was calculated in paper I to be 12.83 eV. The peak maximum is a full 1 eV below the vertical transition energy, which difference reflects the influence of autodetachment upon the nuclear dynamics. The large autodetachment probability weights those components of the propagating wave packet which are closer to the product arrangement, i.e., lower on the potential-energy surface, and results in a breakdown of the multidimensional reflection principle.

The product channel H_2+O^- is the minor one for DEA via the first two resonances, $^2B_1$ and $^2A_1$. We have failed to reproduce the corresponding experimental results; our calculations produce a very small cross section for DEA via the $^2B_1$ resonance to produce this channel, and zero cross section for $^2A_1$. We regard nonlocal effects to be a prime candidate for the physical origin of this channel for the $^2B_1$ state; for the $^2A_1$ state, we suspect that three-body dissociation into $H+H+O^-$, which is not treated in the present study, may play a significant role in this channel.

TABLE II. Attachment widths and survival probabilities calculated for the three resonances using Eqs. (33)–(35).

	Attachment width (10^{-4} a.u.)			Survival probability		
	$^2B_1$	$^2A_1$	$^2B_2$	$^2B_1$	$^2A_1$	$^2B_2$
H_2O	3.47	4.33	4.74	0.938	0.651	0.215
D_2O	3.54	4.19	4.84	0.916	0.572	0.131

The probability of a dissociative attachment event is neatly divided into distinct probabilities for attachment and survival by the local complex potential model. The norm of the driving term in the driven Schrodinger equation of the LCP model, Eq. (10), corresponds to the probability for electron attachment, weighted by the envelope of the initial vibrational state. We define this quantity as the attachment width Γ_A,

$$\Gamma_A = 2\pi\langle\phi_{\nu_i}|\phi_{\nu_i}\rangle, \tag{33}$$

and list the values of Γ_A for each of the resonances in Table II.

Once the electron has attached, the loss of flux via the imaginary component of the complex-valued surfaces determines the survival probability of the anion state. The survival probability may be calculated by integrating the flux $F_{j\nu}(E)$ over energy,

$$P_{\text{surv}} = \frac{\sum_{j\nu}\int dE F_{j\nu}(E)}{\langle\phi_{\nu_i}|\phi_{\nu_i}\rangle}. \tag{34}$$

The calculated survival probabilities are also listed in Table II. The survival probability for the lowest $^2B_1$ resonance state is near 1, and therefore for this resonance the magnitude of the cross section is controlled by the attachment probability. For DEA via the $^2A_1$ state, the cross section is lowered by the effect of autodetachment, though once attached the electron is more likely to survive to dissociation. For DEA via the upper $^2B_2$ resonance, the large majority of the attached wave packet is lost to autodetachment; therefore, the variation of the lifetime of this state with nuclear geometry plays a large role in the dynamics.

We calculate the average degree of rotational and vibrational excitation, as well as the average kinetic energy of the anion recoil, for each of the final channels by weighting the survival probability by the quantity of interest,

$$\langle\nu\rangle = \frac{\sum_{j\nu}\nu\int dE F_{j\nu}(E)}{\langle\phi_{\nu_i}|\phi_{\nu_i}\rangle P_{\text{surv}}},$$

TABLE III. Expectation values of final vibrational quantum number $\langle \nu \rangle$ and angular momentum quantum number $\langle j^2 \rangle$ of diatomic fragment, as well as the expectation value of the kinetic energy of the anion recoil, $\langle E_{\mathrm{kin}} \rangle$, for each resonance, as calculated with Eq. (35). Average kinetic energy determined by the experimental method of Ref. [20], final column.

Diatomic fragment	$\langle \nu \rangle$	$\langle j^2 \rangle$	$\langle E_{\mathrm{kin}} \rangle$	$\langle E_{\mathrm{kin}} \rangle$, Expt.[a]
$^2B_1$ H^-+OH	1.28	107	2.04 eV	0.96 eV (1.5 eV)[b]
H_2+O−	3.52	412	0.154	0.12
D^-+OD	1.75	240	1.89	0.70
D_2+O−	3.34	821	0.125	0.14
$^2A_1$ H^-+OH (K=0)	2.11	121	3.35	1.55 (2.5 eV)[b]
D^-+OD (K=0)	2.98	221	3.16	1.20
$^2B_2$ H^-+OH ($^2\Pi$)	[c]	[c]	[c]	
H^-+OH ($^2\Sigma$)	4.69[c]	439[c]	3.45[c]	
H_2+O−	7.75	405	0.413	0.57
D^-+OD ($^2\Pi$)	[c]	[c]	[c]	
D^-+OD ($^2\Sigma$)	6.63[c]	819[c]	3.35[c]	
D_2+O−	13.0	725	0.684	0.79

[a]Data from Ref. [20], except where noted.
[b]Ref. [9].
[c]The calculation for H^- production via $^2B_2$ is not converged.

$$\langle j^2 \rangle = \frac{\sum_{j\nu} j(j+1) \int dE F_{j\nu}(E)}{\langle \phi_{\nu_i} | \phi_{\nu_i} \rangle P_{\mathrm{surv}}},$$

$$\langle E_{\mathrm{kin}} \rangle = \frac{\sum_{j\nu} \frac{M_{\mathrm{diatom}}}{M_{\mathrm{total}}} (E_{\mathrm{inc}} - E_{j\nu}) \int dE F_{j\nu}(E)}{\langle \phi_{\nu_i} | \phi_{\nu_i} \rangle P_{\mathrm{surv}}}. \quad (35)$$

In the third line of Eq. (35), E_{inc} is the incident electron energy, $E_{j\nu}$ is the energy of the final state relative to the ground vibrational state of H_2O, and M_{total} and M_{diatom} are the masses of the original triatom and the diatomic fragment, respectively, so that the resulting quantity is the kinetic energy of the anion recoil in the laboratory frame. We present these results in Table III, along with experimental data on the anion recoil kinetic energy from Fedor *et al.* [20].

Our calculated average values of the anion recoil kinetic energy, $\langle E_{\mathrm{kin}} \rangle$, agree to varying degrees with the results of Ref. [20]. Our calculated values for average kinetic energy release for the production of H^- from the $^2B_1$ and $^2A_1$ resonances are much larger than observed by these authors, but closer to the values measured by Belic *et al.* [9]. As described in paper I, the potential-energy surfaces that we have constructed for these resonance states reproduce the energetics of the two-body asymptotes very well (to within 0.08 eV for the ground vibrational state). Errors in the present results may therefore only come from errors in the vertical transition energies, or a misrepresentation of the dynamics prior to breakup. As discussed above, it is likely that our vertical transition energies for the $^2B_1$ and $^2A_1$ resonances are too high, perhaps by as much as 0.4 eV relative to the proper physical values. Most of this excess energy may be transmitted to the kinetic energy of the H^- recoil, due to the small mass of hydrogen relative to the H_2O molecule. While our calculated results exceed the experimental result of Ref. [20] by more than 0.4 eV, they are within 0.4 eV of the Belic *et al.* value for the $^2B_1$ state and 0.85 eV for the $^2A_1$ state. Fedor *et al.* comment that the values obtained for the kinetic energy release of H^- via the $^2B_1$ and $^2A_1$ resonances by Belic *et al.* [9] "may be considered as more accurate." The discrepancy with Belic *et al.* for the $^2B_1$ result supports our recommendation that the physical transition energy for the $^2B_1$ state be taken to be approximately 6.2 eV. The maximum kinetic energy release at our calculated peak locations of 6.87 and 8.74 eV for the $^2B_1$ and $^2A_1$ states, is, respectively, 2.38 and 4.15 eV. Our results are therefore very near the maximum values and reflect the small average degree of vibrational excitation that we calculate.

Our values for the average kinetic energy release of the major O^- fragment from the $^2B_2$ resonance agree much better with the results of Fedor *et al.*; we again underestimate the experimental result, but only by 28% and 13%, respectively, for the nondeuterated and deuterated target. For this channel, the degree of excitation of the H_2 (D_2) fragment is large, and therefore the kinetic energy of the atom-diatom recoil is less than its maximum allowed value. The maximum kinetic energy release at our calculated peak (11.75 eV) is 0.91 eV, more than twice our result for the average value. Therefore, more energy goes into the rovibrational excitation of the H_2 fragment than into the kinetic energy of the recoil.

We do not calculate the three-body dissociative electron attachment cross section, i.e.,

$$H_2O + e^- \rightarrow \begin{cases} H + H + O^-, & 8.04 \text{ eV} \\ H^- + H + O, & 8.75 \text{ eV}. \end{cases} \quad (36)$$

The complex absorbing potential flux formalism [50,51,56] that is employed within the MCTDH implementation [52] is not appropriate for the three-body breakup channel, at least when used in conjunction with the Jacobi coordinate systems used here. We do, however, produce rigorous results for the two-body channels by projecting upon the bound rovibrational final states as in Eq. (27) and summing.

Our surfaces, as described in paper I, are not designed to reproduce the dynamics leading to three-body dissociation either. Due to our neglect of the shape or Feshbach resonance intersection on the $^2B_2$ manifold, which is a true characteristic of the physical system and which leads to the double-valuedness of the physical surface, we cannot accurately represent the dynamics leading to the three-body dissociation channels with our single $^2B_2$ surface. The $^2B_2$ manifold is coupled to the $^2A_1$ state in the three-body region by the conical intersection, and therefore it is possible that this omission affects the dynamics via the $^2A_1$ state as well.

It is clear that we may only rigorously compare our results with experiment for the two-body channels. The comparison is complicated by the fact that the experimental results are

sometimes not final-channel resolved, such as those presented in Fig. 3, and in any case always incorporate a finite resolution in determining the energy of the incident electron energy and the kinetic energy of the recoil. The energetics of the asymptotes of the physical surfaces, which are mirrored very well by our constructed potential-energy curves, dictate that for the lowest $^2B_1$ state the three-body channels are closed, but that for DEA via the other two resonances, at least one three-body channel is open.

In the following subsections, we give the principal findings of the nuclear dynamics calculations for each channel that was studied. Further details are given in the EPAPS archive [60]. Most calculations were carried out for the ground vibrational state and for total rotational angular momentum $J=0$ (or, in the case of the Renner-Teller coupled $1\ ^2A'-^2B_1$ calculations, $R_z=0$). Rovibrationally excited initial states were also examined, and these are listed in the descriptions of the individual calculations which follow.

A. Dissociative electron attachment via the $^2B_1$ state

We have previously [16,17] performed a calculation on the $^2B_1$ state, which is superseded by the present treatment. We perform the calculation using the one uncoupled $^2B_1$ potential-energy surface. We have confirmed that Renner-Teller coupling to the $^2A_1$ state at linear geometry has a negligible effect on the dynamics, at least for DEA via the ground rovibrational state of the target.

The treatment in our previous study [16,17] was not able to resolve the cross section in the minor O^-+H_2 channel ($\frac{1}{40}$th of the major channel), due to deficiencies in the potential-energy surface. While the present study does obtain converged O^-+H_2 cross sections, they are two orders of magnitude below the observed cross sections, and peak at energies well above the experimental peaks; it is therefore clear that we have not represented the dynamics leading to this minor channel accurately. In this regard, this may be due to small deficiencies in the potential-energy surface, or to the presence of significant nonlocal effects in this minor channel.

In the previous study, we reproduced the magnitude of the $OH+H^-$ cross section to within a few percent. We continue to regard that close agreement to be essentially fortuitous. Apart from an overall scale factor, the present calculations for production of H^- reproduce the shape and energy dependence of the experimental results very well. It appears that the current value calculated for the width of the $^2B_1$ resonance at the equilibrium geometry of the neutral, 10.31 meV, is larger than the physical value, the latter being closer to our previously calculated value of 6.0 meV. It is likely that a more accurate description of electron correlation than we could include in the complex Kohn calculations of paper I is required to reproduce the resonance wave function of the $^2B_1$ state.

1. Production of OH ($X\ ^2\Pi_1$)+H^- via $^2B_1$ state

This is the dominant channel for DEA to H_2O, having a peak cross section of approximately 6×10^{-18} cm^2. Cross sections as a function of incident electron energy are shown in Fig. 4. We calculate a peak cross section of 10.35 $\times10^{-18}$ cm^2 at 6.87 eV. The magnitude of this cross section is larger than the experimental value (6.6×10^{-18} cm^2), and the location of the peak is displaced upward by 0.4 eV. For this resonance, autodetachment is nearly negligible. Therefore, the excess in the magnitude that we calculated reflects the fact that the calculated width values, and hence the entrance amplitudes, are too large.

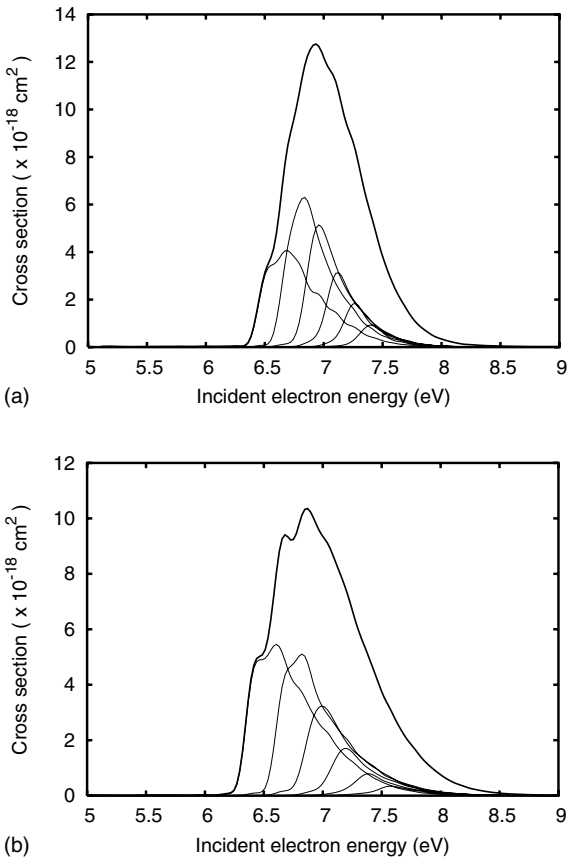

FIG. 4. Cross sections for production of H^-+OH (ν), left, or D^-+OD (ν), right, from $^2B_1$ state as a function of incident electron energy. Total, thick line; vibrational states 0 (ground) through 5, thinner lines.

The cross sections in Fig. 4 are very similar in shape to those produced previously [16,17], though they are larger in magnitude. At low incident electron energies, the first vibrational state is produced exclusively, and subsequent vibrational states have sharp onsets. As the degree of vibrational excitation increases beyond the first few quanta, the magnitude of the cross section decreases. Despite the fact that the first five excited vibrational states are clearly visible in Fig. 4, the average number of quanta excited is only 1.28. The average kinetic energy release, therefore, is near its maximum value of 2.38 eV. The degree of rotational excitation calculated for this state is relatively low ($\langle j^2\rangle=107$ for H_2O).

A two-dimensional view of the data is provided in Fig. 5, where the kinetic energy of the anion recoil, as determined by a full final-state resolution of the products, is plotted versus incident electron energy; the contour lines indicate the magnitude of the cross section. The kinetic energy of the anion recoil in the laboratory frame is

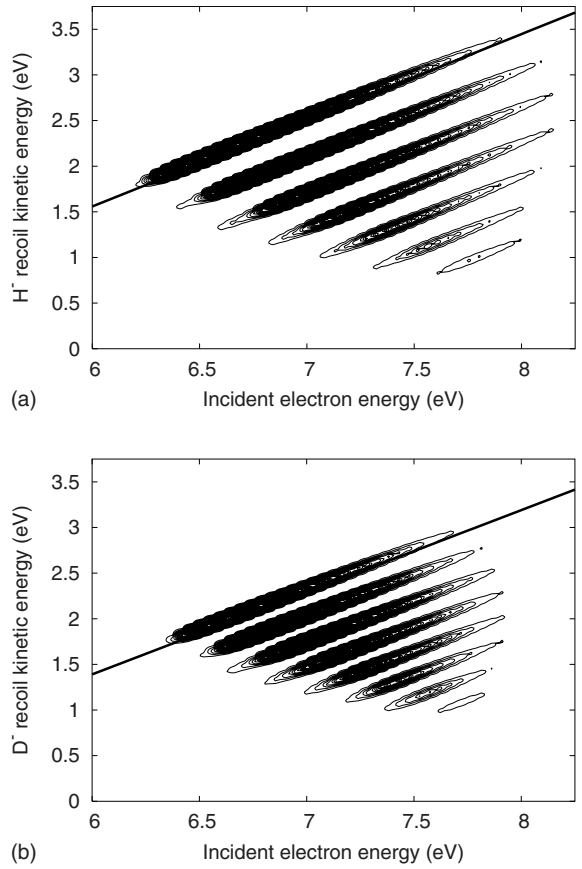

FIG. 5. Left, cross section for production of H^-+OH from $^2B_1$ resonance as a function of incident electron energy and H^- fragment kinetic energy, unshifted, with the physical value of the maximum kinetic energy available plotted as a bold line. The contour lines indicate the magnitude of the cross section. Right, deuterated results. The physical value for the maximum kinetic energy is slightly lower than the value corresponding to our calculated surfaces. Contours every 2×10^{-17} cm^2 eV^{-1}.

$$E_{\mathrm{kin/anion}} = \frac{M_{\mathrm{diatom}}}{M_{\mathrm{total}}}(E_{\mathrm{inc}} - E_{j\nu}), \tag{37}$$

as in Eq. (35). This figure shows that the degree of rotational excitation for production of both H^-+OH and D^-+OD is small compared to the vibrational spacing of the OH fragment, because there are separate lobes corresponding to each vibrational state. For the deuterated case, the lobes are thicker and closer together. The thick line in this figure corresponds to the maximum kinetic energy available, as determined by the physical energetics of the system; the maximum kinetic energy as determined by the energetics of the constructed surface is slightly higher.

In Fig. 6, we plot the cross section as a function of H^- recoil kinetic energy for several values of incident electron energy. To compare with the experimental results of Belic, Landau, and Hall [9], which reflect the finite resolution of the kinetic energy of the anion recoil, we incorporate the experimental resolution of 150 meV in the ion kinetic energy direction. Such resolution effectively smears each vibrational peak into the next, and there are no hard zeros visible in the

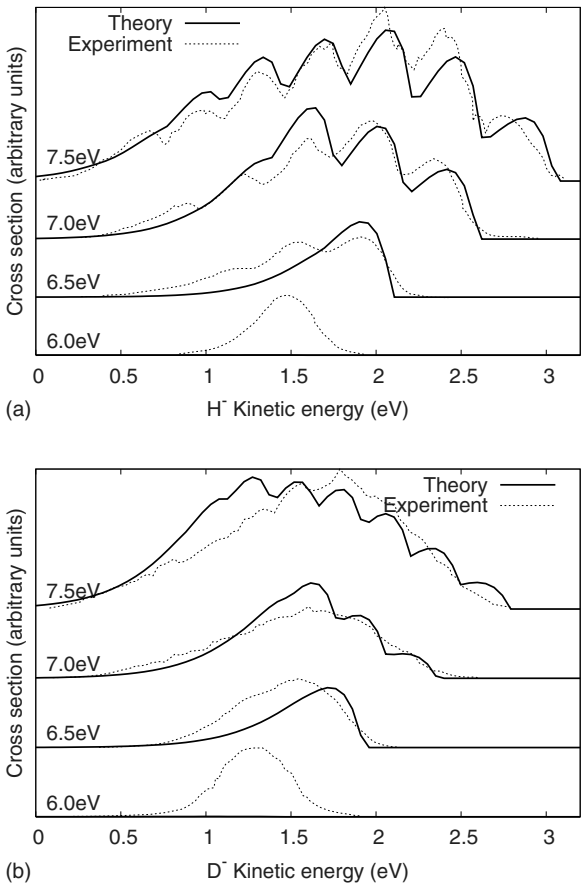

FIG. 6. Left, production of H^-+OH via the $^2B_1$ resonance at different incident electron energies, as a function of H^- fragment kinetic energy, unshifted, on arbitrary and different scales for each incident electron energy. Right, D^-+OD. Calculated results have been broadened using a 150 meV linewidth, consistent with the plotted experimental results from Belic, Landau, and Hall [9].

data of Fig. 6. A key result of our calculation is that with better experimental resolution, the individual vibrational peaks should be able to be resolved, not only for H_2O, but also for D_2O, and that these peaks should be fully separated. The experimental resolution of Ref. [9] was insufficient to delineate the separate vibrational peaks for D_2O. We doubt that these authors have resolved the rotational structure for H^-+OH production at 7.5 eV incident electron energy, as they claim.

The isotope effect observed for this channel has been a matter of some interest. Compton and Christophoreau [5] observed the ratio of peak heights for the deuterated (D_2O) to the nondeuterated (H_2O) species to be 0.75, and the ratio of the energy-integrated cross sections, which approximate the ratio of survival probabilities P_{surv} calculated with Eq. (35), to be 0.60. In contrast, we observe a larger peak for the deuterated species, and similar survival probabilities P_{surv}, both near 1.

The recent results of Fedor *et al.* [20] resolve this discrepancy. The peak heights that they obtain for H^-+OH production versus D^-+OD production via the $^2B_1$ resonance indicate a *larger* peak for D^-+OD, reversing the prior experimental evidence, and putting experiment and theory on

qualitatively similar ground. It is clear that the ratio of peak heights obtained by Fedor *et al.*, while not explicitly calculated by these authors, is nearer to 1 than the present theoretical results, but it is reassuring that the trend for both experiment and theory is in the same direction. The combination of the results of Ref. [20] and the present results indicates that the survival probability for the physical $^2B_1$ state is indeed near 1, and that minimal flux is lost via the autodetachment for DEA via this resonance.

The propagated wave packet, a plot of which can be found in the EPAPS archive [60], gives a qualitative explanation of the peaks observed in the left panel of Fig. 4. An analysis of this behavior was given in our earlier study [17]. For the deuterated version, the peaks are not discernible. This is due to the larger reduced mass in the symmetric stretch direction, which causes the peaks to lie on top of one another.

2. Production of H_2+O^- via the $^2B_1$ state

This channel is by far the minor channel for DEA via the $^2B_1$ resonance. The peak of the H_2+O^- cross section is approximately 1/40th the height of the peak for the major H^- +OH channel [6]. Being such a minor channel, it presents a more difficult challenge for theoretical methods such as MCTDH, and a greater test for the local complex potential model. We were able to obtain converged cross sections with the present treatment, although the magnitudes of our calculated values are far below the experimental results. Therefore, it is clear that we have not represented the dynamics into this channel accurately. It is possible that minor errors in our calculated surface are to blame, or that the LCP model is inadequate.

We present the cross sections calculated for H_2+O^- production as a function of incident electron energy in Fig. 7. We compare the total cross section for H_2 production from H_2O with that for D_2 production from D_2O in the left panel of this figure. The cross sections peak at 7.6 eV, 0.5 eV above the experimental peak at 7.1 eV, and are far smaller than the experimental result. Although our representation of the nuclear dynamics leading to this channel is clearly lacking, we performed additional calculations in which the target state of H_2O was rovibrationally excited. We performed two calculations for total angular momentum $J=5$, employing the centrifugal sudden (CS) approximation with $K=0$, in the R-embedding coordinate system, as well as a calculation with $J=0$ but one quantum of bend, the (010) state. The total cross sections for production of H_2 from these excited states are compared to the ground initial state result in the right panel of Fig. 7.

As is clear from these results, initial excitation of the target may play a large role in determining the magnitude of the DEA cross section for H_2+O^- production via the $^2B_1$ state, but it is insufficient to explain the discrepancy between the theoretical and experimental results. The effect of bending excitation increases the cross section dramatically; rotational excitation to $J=5$ also enhances the cross section by approximately a factor of 2. The excitation energy of the bending mode is approximately 0.2 eV; that of the $J=5$, $K=0$ state is approximately 0.056 eV. These quantities may be

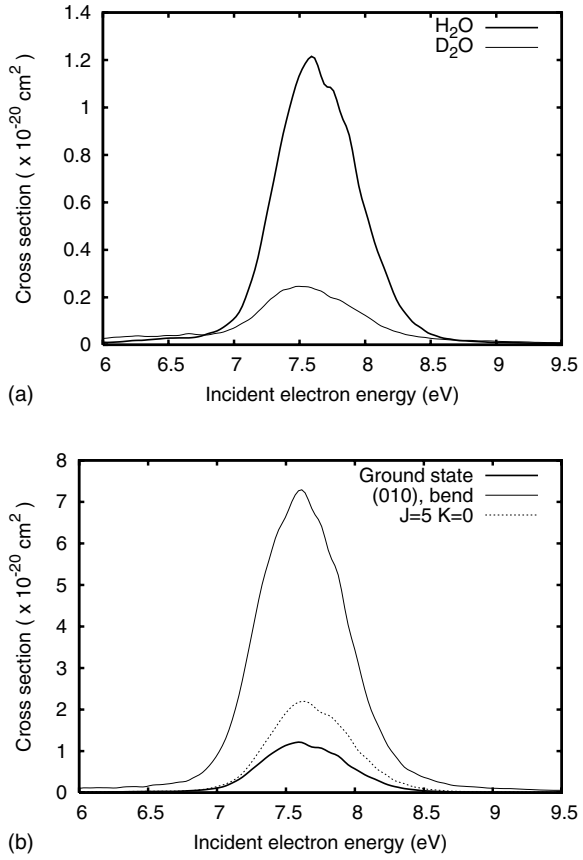

FIG. 7. Cross sections calculated for production of H_2+O^- via the $^2B_1$ state as a function of incident electron energy. Left, calculated isotope effect: comparison of H_2O and D_2O. Right, effect of target excitation: ground initial state result is compared to the result from the (010) target state with one quantum of bend and to the result from $J=5$, $K=0$.

compared to the value of kT at 373.15°K, which is 0.032 eV. This comparison indicates that the bending state is not significantly populated in typical experimental setups and should not be responsible for the magnitude of the observed cross sections. Comparison of the rotational energy to kT indicates that the degree of rotational excitation of the target may determine the precise value of the peak cross section observed in experiment. However, rotational excitation of the sample is insufficient to explain the discrepancy between our results and the experimental ones. For the R-embedding coordinate system, the $K=0$ projection of angular momentum is the most likely to enhance the DEA cross section for production of H_2, because that projection minimizes the centrifugal potential in the r_{HH} coordinate [see Eq. (17)]. The calculated enhancement is due to the effect of the centrifugal potential in R, which "pushes" the wave packet toward large R, where the O^-+H_2 potential well lies.

Because the width Γ of the $^2B_1$ resonance is small for all nuclear geometries, one might expect any nonlocal effects in the resonant nuclear dynamics to be small as well. However, we are considering here a minor channel, which is only barely accessible with LCP dynamics on the constructed potential-energy surface. If nonlocal effects were to open a new dynamical pathway, or otherwise effectively lower the

dynamical barrier to the H_2+O^- well, the magnitude of such effects would not have to be great in order to produce a noticeable enhancement of such a small cross section. Therefore, we regard nonlocal effects to be a strong candidate for the source of the experimentally observed cross section for production of H_2+O^- via the $^2B_1$ resonance.

B. Dissociative electron attachment via the $^2A_1$ ($1\ ^2A'$) state, Renner-Teller coupled to the $^2B_1$ state

These calculations are performed in the diabatic ($l_z=\pm 1$) basis, which diagonalizes the nuclear kinetic energy operator with the Renner-Teller effect, as per the discussion in Sec. IV, employing the centrifugal sudden Hamiltonian of Eq. (17). The initial state is the adiabatic $^2A_1$ ($1\ ^2A'$) state, comprised of equal parts $l_z=\pm 1$. Like the other calculations we present that incorporate rotational motion, they are parametrized by the body-fixed angular momentum quantum number K, which is the projection of the total angular momentum onto the embedding axis. However, for these Renner-Teller calculations, K is interpreted as the eigenvalue of the projection of the nuclear rotational angular momentum R_z, not the total angular momentum J_z, upon the embedding axis, and therefore the diabatic basis $l_z=\pm 1$ corresponds to $J_z=K\pm 1$ [61].

We have obtained cross sections for the major H^-+OH ($X\ ^2\Pi$) channel of DEA via the $^2A_1$ resonance. However, for the minor H_2+O^- channel, we have not been able to obtain converged, nonzero cross sections. The mechanism for DEA via the $^2A_1$ resonance to produce H_2+O^- remains unknown. It is possible that three-body breakup, which we have not treated, is important here.

The considerations of Ref. [18] indicate that the nuclear dynamics of DEA via the $^2A_1$ resonance may hold some surprises, and that the LCP model may be insufficient for a full description thereof. In particular, as demonstrated in paper I, the width of the $^2A_1$ resonance becomes large as the nuclear geometry moves toward the H^-+OH product arrangement. We have calculated width values as high as 0.15 eV for this resonance state for such stretched geometries, despite the fact that the resonance state lies only slightly above the neutral at these geometries and ultimately becomes bound as the atom-diatom distance is further increased. The explanation for this behavior is that the electronic structures of the neutral and anion become highly correlated and different from each other at such stretched geometries, and as a result, there is considerable shape resonance character mixed into the $^2A_1$ Feshbach resonance. The radically peaked behavior of the width of the $^2A_1$ state may portend a breakdown of the LCP, model which relies on the implicit assumption that the background-resonance coupling is a relatively smooth function of nuclear geometry. Also, the fact that the $^2A_1$ resonance is coupled to the neutral target by an s-wave matrix element indicates that virtual state effects may play a large role as the resonance becomes bound. Such virtual state effects cannot be properly described by the LCP model, but have been taken into account in other systems using effective range theory as, for example, in Refs.[62,63]. The fact that we have overestimated the magnitude of the experimental cross section for H^-+OH production via the $^2A_1$ resonance indicates that a breakdown of the LCP model may be responsible for the loss of flux via autodetachment.

1. Production of H^-+OH via the Renner-Teller coupled $^2A''$ ($^2B_1$) and $1\ ^2A'$ ($^2A_1$) states

The cross sections for total H^-+OH production were easy to converge, as the channel involved is the main channel, the dissociation direct, and the dynamics apparently reasonably separable in the r_{OH} Jacobi internal coordinate system. The relatively small size of the single-particle function (SPF) expansions required to converge the calculation (see the EPAPS archive) support this conclusion. We found the Renner-Teller coupling to have a negligible effect on both the magnitude of the total cross section and its breakdown into rotational and vibrational states, so we only report results for $K=0$. The cross sections (for $K=0$) into final vibrational and rotational levels of the diatomic fragment, for both the deuterated and nondeuterated cases, are given in the EPAPS archive.

Our theoretical treatment overestimates the cross section for DEA into this channel via the $^2A_1$ resonance. Our peak heights (see Table I), 4.14 and 4.16×10^{-18} cm^2 for the nondeuterated and deuterated target, respectively, are approximately three times larger than Melton's observed peak height of 1.3×10^{-18} cm^2. Although the recent results of Fedor *et al.* [20] do resolve this peak better than previous experiments, and indicate that Melton's peak height value may be too low, there is a clear discrepancy between theory and experiment here. We attribute the discrepancy to virtual state effects, as discussed in Ref. [18], which may lead to significant autodetachment as the $^2A_1$ ($1\ ^2A'$) state becomes bound. There is also the possibility that we have overestimated the entrance amplitude for this state, as we have done for the$^2B_1$ state.

The degree of vibrational excitation is higher for this resonance than for the $^2B_1$ resonance: the values of $\langle v\rangle$ calculated from Eq. (35) are 2.03 and 1.28 for the $^2A_1$ and $^2B_1$ resonances, respectively. This difference is most likely due to the gradient of the potential-energy surface in the symmetric stretch direction, which is larger at the equilibrium geometry of the neutral for the $^2A_1$ surface than for the $^2B_1$ surface. The behavior of the propagated wave packet, which is plotted in the EPAPS archive, is similar to that found for the $^2B_1$ resonance: the wave packet experiences an initial impulse in the symmetric stretch direction, but then is bifurcated by the developing potential wall in this direction, and reflected into either H^-+OH channel. The vibrational excitation is the result of the wave packet oscillating in the r direction as it passes down the OH potential well.

The degree of rotational excitation within the OH fragment is also higher for the $^2A_1$ state than for the $^2B_1$ state. Using Eq. (35), we calculate an average degree of rotational excitation $\langle j^2\rangle = 119$ for this resonance, compared to 107 for the $^2B_1$ resonance. This results from the larger gradient of the potential-energy surface in the bend direction for the $^2A_1$ surface compared to the $^2B_1$ surface. The $^2A_1$ wave packet is given an impulse in the bend direction, which corresponds to excitation of rotational quanta j. This excitation persists in the final state, as demonstrated by these calculations.

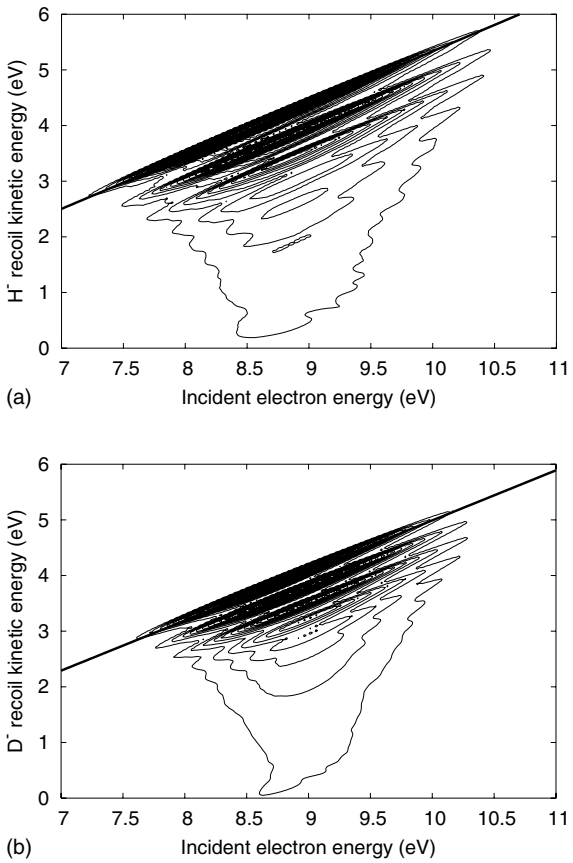

FIG. 8. Left, production of H^-+OH from the $^2A_1$ state, as a function of incident electron energy and H^- fragment kinetic energy, as in previous plots; right, deuterated. The maximum kinetic energy available, as determined from the physical energetics, is plotted with a bold line. Contours every 6×10^{-18} cm^2 eV^{-1}.

Figure 8 presents two-dimensional plots of the cross section as a function of both incident electron energy and final anion recoil kinetic energy. Figure 8 displays a clear difference from Fig. 5. This figure shows that for DEA via the $^2A_1$ state, the degree of rotational excitation of the diatomic fragment is high enough that the different vibrational states are distinguishable, but not completely separated.

We compare our results for the laboratory-frame, anion recoil kinetic energy distribution at an incident electron energy of 8.5 eV with the corresponding results of Belic, Landau, and Hall [9] in Fig. 9. (Two-dimensional plots of the cross section as a function of both incident electron energy and final anion recoil kinetic energy can be found in the EPAPS archive.) In contrast to the case of H^- production from the $^2B_1$ state, here the degree of rotational excitation of the diatomic fragment is high enough that the different vibrational states are distinguishable, but not completely separated. The experimental resolution of Ref. [9] was insufficient to delineate the different peaks for various OH (ν), although our calculations demonstrate that with sufficient resolution, the vibrational structure should be apparent. In Fig. 10, we compare to the experimental results of Curtis and Walker [10].

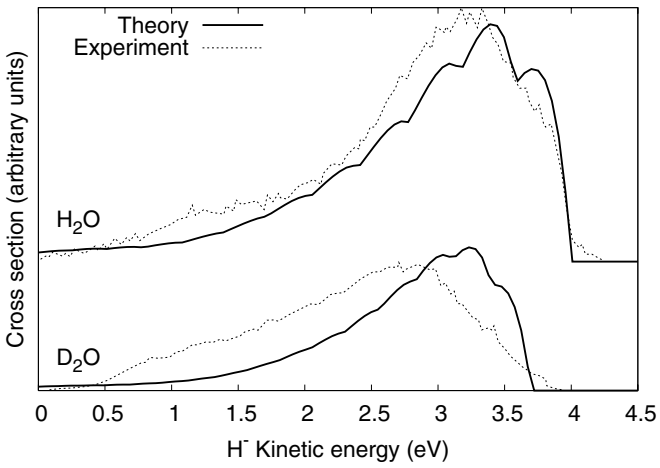

FIG. 9. Production of H^-+OH ($^2\Pi$) and D^-+OD ($^2\Pi$) via the $^2A_1$ state at 8.5 eV incident electron energy, as a function of fragment kinetic energy, as in previous plots. Calculated results have been broadened using a 150 meV linewidth to compare with the experimental results from Belic, Landau, and Hall [9], also plotted.

2. *Failure to calculate production of* H_2+O^- *via dissociative attachment to the* $^2A_1$ *state*

We have been unable to obtain a nonzero cross section for DEA via the $^2A_1$ ($1\ ^2A'$) state, Renner-Teller coupled to the $^2B_1$ state, leading to H_2+O^-. We have attempted calculations for $K=0$ (uncoupled), 1, 2, 3, and 4. Within the MCTDH calculations, we employed single-particle function (SPF) expansions of up to $24\times36\times30$, with no success. With this large SPF expansion, and propagation times of up to 100 fs, we regard the representation of the LCP dynamics within the MCTDH ansatz to be accurate. We suspect that O^- production from $^2A_1$ may be dominated by three-body breakup into $H+H+O^-$, which we have not treated.

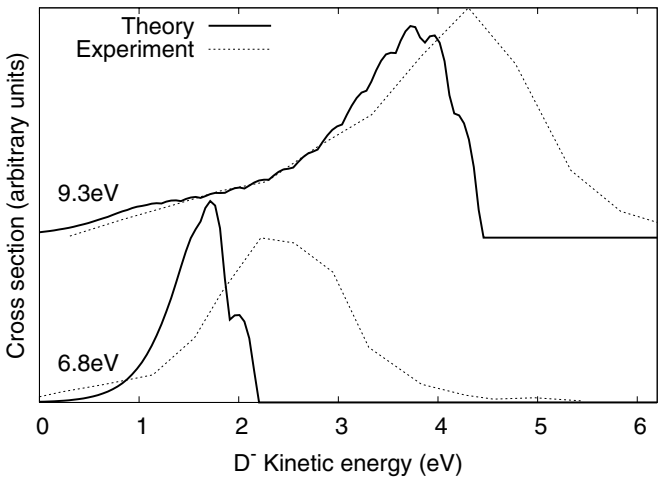

FIG. 10. Production of D^-+OD ($^2\Pi$) at 9.3 eV ($^2A_1$) and 6.8 eV ($^2B_1$), as a function of D^- fragment kinetic energy, as in previous figures, with experimental results from Curtis and Walker [10].

C. Dissociative electron attachment via the $^2B_2$ state, involving the conical intersection with the $^2A_1$ state

As described in Ref. [18] and paper I, dissociative electron attachment to H_2O via the highest-energy $^2B_2$ state must involve the conical intersection that this state exhibits with the $^2A_1$ state. The gradient of the potential-energy surface leads directly toward this conical intersection from the equilibrium geometry of the neutral. The conical intersection forms a line in the three-dimensional space of nuclear geometries, and occurs within C_{2v} symmetry, where the OH bond lengths are equal.

We performed a diabatization on the results of configuration-interaction calculations on $^2A_1$ and $^2B_2$ (1 and 2 $^2A'$) resonances, as described in paper I, to produce a set of diabatic $^2A_1$ and $^2B_2$ surfaces along with a coupling surface. These diabatic surfaces are employed in all of the following calculations.

Before describing the individual calculations, a few preliminary remarks about the experimental observations are in order. Although absolute cross sections for H^- production via the $^2B_2$ resonance are not available, the experimental evidence [6,20] indicates that for both D_2O and H_2O target states, the branching ratio between H^- production and O^- production highly favors O^-. Therefore, the dynamics of DEA beginning in the $^2B_2$ state are much different from those for the lower-energy $^2A_1$ and $^2B_1$ resonances, which yield far more H^- than O^-.

This observation is not surprising, in light of the potential-energy surfaces that we have calculated and shown in paper I; the upper 2 $^2A'$ surface was demonstrated to be quite different from those of the lower resonances. In particular, the dynamics beginning on the $^2B_2$ (2 $^2A'$) surface will begin with a decrease of the H-O-H bond angle θ_{HOH}, which motion will favor the H_2+O^- product arrangement. However, as we will show, there appears to be active competition between the two product arrangements, and the branching ratio observed in experiment is likely the product of both the shape of the real-valued component to the 2 $^2A'$ surface and the behavior of its imaginary component.

As is clear from Table I, the cross sections we calculate for this channel are smaller than the observed cross sections. However, the comparison is complicated by the fact that the three-body dissociation channels are open for incident electron energies sufficient to reach the $^2B_2$ resonance, and we produce cross sections only for the two-body dissociation channel; the disagreement may therefore be due to a large contribution of the three-body breakup channel to the dominant production of O^-. However, the locations of the calculated and experimental peak maxima for production of O^- from the $^2B_2$ resonance agree very well: both cross sections peak at about 11.8 eV. Although the presence of the three-body dissociation channel may shift the peak, this comparison indicates that we have probably accurately represented the vertical transition energy for the $^2B_2$ resonance. The vertical transition energy as represented by our configuration-interaction surface is 12.83 eV, and therefore we recommend a value of approximately 12.8 eV for the appropriate physical transition energy. This value is above the value of 11.97 eV given by the complex Kohn calculations of paper I.

The calculated branching ratio between H_2+O^- (D_2+O^-) and $OH+H^-$ ($OD+D^-$) production is near unity but the experimental ratio (for the undeuterated product) exceeds 1 by a large factor. As we will show, the dynamics within the first few femtoseconds after attachment are controlled by both real and imaginary components of the potential-energy surface, the latter consuming most of the propagated wave packet within the first six femtoseconds.

We have examined the effect of rotational excitation upon the cross section for production of H_2+O^- from DEA via the $^2B_2$ state, and find it to be negligible.

1. *Production of* H^-+OH ($^2\Pi$ or $^2\Sigma$) *via the upper* $^2B_2$ *state*

The calculation for the production of OH ($^2\Pi$ or $^2\Sigma$) $+H^-$ via the $^2B_2$ Feshbach resonance, which is coupled to the $^2A_1$ resonance via their conical intersection, proved difficult to converge. This is evidenced by raggedness in the OH ($^2\Pi$) channel cross sections. A final-state resolution in this channel was not possible, although we were able to resolve the final states of OH ($^2\Sigma_2$).

With reference to the discussion in Ref. [18] and paper I, the constructed diabatic $^2B_2$ surface correlates to the species H^-+OH ($^2\Sigma$), as does the adiabatic $^2B_2$ (2 $^2A'$) surface. The diabatic $^2A_1$ surface correlates to H^- plus ground state OH ($^2\Pi$), as does the adiabatic 1 $^2A'$ state. Therefore, dynamics beginning on the $^2B_2$ surface that leads to production of the ground-state H^-+OH ($^2\Pi$)species must proceed via the off-diagonal coupling to the $^2A_1$ surface. From the viewpoint of the diabatic basis, the off-diagonal coupling must in this case lead to a transition between the diabatic $^2B_2$ and $^2A_1$ surfaces; from the viewpoint of the adiabatic basis, the dynamics must proceed through the conical intersection via the singular derivative couplings inherent in that basis.

We present the calculated total cross sections for production of either H^-+OH or D^-+OD in Fig. 11. The results are similar in shape, but the magnitude of the cross sections for the deuterated case is approximately half that of the nondeuterated case. Differences in the reduced masses in the dissociative direction result in a relatively longer time during which the deuterated species may undergo autodetachment and, consequently, a smaller survival probability for the deuterated anion. As shown in Table II, the survival probability for the nondeuterated $^2B_2$ state is 0.215, whereas for the deuterated species it is only 0.131. Unfortunately, there are no experimental data for comparison that measure the relative magnitude of the H^- and D^- peaks for the highest-energy $^2B_2$ resonance.

An obvious feature of the results presented in Fig. 11 is that the branching ratio of OH ($^2\Pi$) to OH ($^2\Sigma$) production depends on the incident energy of the electron. This ratio varies from 1 (only $^2\Pi$ is produced) at onset to zero (only $^2\Sigma$ produced) at higher energy. At low energy, the observed cross section is the result of dynamics in which the wave packet makes a nonadiabatic transition from the upper $^2B_2$ (2 $^2A'$) surface to the lower $^2A_1$ (1 $^2A'$) surface, whereas at high energy, the observed cross section is due to dynamics in which there is no transition. Thus, the nuclear dynamics via the $^2B_2$ state involve the conical intersection to produce a

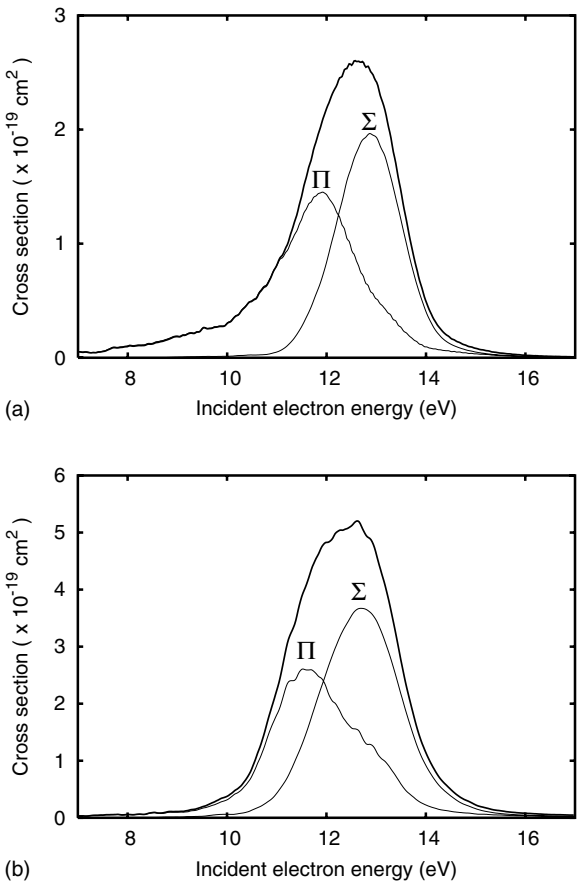

FIG. 11. Left, total cross section calculated for production of H^-+OH ($^2\Pi$) vs H^-+OH ($^2\Sigma$) from the $^2B_2$ state as a function of incident electron energy. Right, deuterated version.

branching ratio that varies with incident electron energy in an interesting way.

We have only been able to achieve final-state resolution for the OH ($^2\Sigma$) fragment. Two-dimensional views of the cross sections for H^-+OH ($^2\Sigma$) production, as a function of both the incident electron energy and the kinetic energy of the H^- fragment, are given in the EPAPS archive, along with comparisons of our calculated results with previous experiment. Our calculations reproduce the approximate level of excitation within the diatomic fragment, as the theoretical and experimental results are both centered near the same kinetic energy, ~2.75 eV for H^- from H_2O, and ~1.5 eV for D^- from D_2O. We cannot make a more quantitative comparison, because there are no experimental values for the average kinetic energy release in this channel.

The wave-packet dynamics for DEA leading to H^- production via the coupled $^2B_2$ or $^2A_1$ states are shown in Figs. 12 and 13. The former shows the reduced density on the adiabatic 1 $^2A'$ surface, the latter on the adiabatic 2 $^2A'$ surface. These plots were obtained by transforming the propagated wave packets from the diabatic basis to the adiabatic basis. The wave packet initially has no magnitude on the lower 1 $^2A'$ surface. Nonadiabatic coupling changes this situation as the wave packet is propagated. The norm of the propagated wave packet on the 1 $^2A'$ surface reaches a maximum of 0.112 at $t=9.1$ fs, by which time a portion of the wave packet has reached the dissociative H^-+OH ($^2\Pi$) well of the 1 $^2A'$ surface. The portion of the wave packet within this well (see the bottom-left panel of Fig. 12) lies beyond the value ($R=4.5a_0$) where the resonance becomes bound, and so it continues toward dissociation with a negligible loss of flux. The subsequent decrease of the norm of the wave packet on the 1 $^2A'$ surface is therefore due to the consumption of other parts of the wave packet by the imaginary component of this surface, and to its absorption by the complex absorbing potentials.

As described in paper I, the magnitude of the width for the upper 2 $^2A'$ surface is generally large, though it decreases slowly as the H^-+OH ($^2\Sigma$) well is approached, and abruptly as the H_2+O^- well is approached. As a result, the wave packet that begins on the upper 2 $^2A'$ surface is rapidly consumed, and its norm decreases from exactly 1 to 0.321 within 6 fs. At this time, the combined norm on both surfaces is 0.402. The calculated total survival probability for this resonance, P_{surv}, calculated with Eq. (34), is 21.5% (see Table II). From this comparison we can see that the majority of the autodetachment for this resonance occurs within the first 6 fs; its survival probability is 40.2% within this initial time period, and 21.5/40.2=53.5% thereafter.

The high degree of vibrational excitation ($\langle\nu\rangle$) in both the OH (Π) and OH (Σ) channels is apparent in the oscillations of the dissociating wave packet within each potential well, visible in the lower panels of Figs. 12 and 13. Figure 12 shows that in this case there is additional structure to the dissociating wave packet on the lower 1 $^2A'$ surface; however, this structure is most likely due to the calculation not being fully converged.

2. Production of H_2+O^- via the upper $^2B_2$ state

The channel H_2+O^- is the dominant channel observed in experiment for dissociative attachment to water via the highest-energy $^2B_2$ resonance. As discussed at length in Ref. [18] and paper I, this channel is not present as an asymptote on the $^2B_2$ (2 $^2A'$) surface, and therefore the system must undergo a nonadiabatic transition via the conical intersection to the lower 1 $^2A'$ surface in order to reach this product channel. In the context of the representation that we constructed in paper I, the system must follow the *diabatic* $^2B_2$ surface past its crossing with the $^2A_1$ diabatic surface. The H_2+O^- channel is present as an asymptote of the diabatic $^2B_1$ surface. As described in Ref. [18] and paper I, the adiabatic $^2A_1$surface does not have a bound asymptote in this arrangement; it correlates to O^-+H_2 ($\sigma_g^1\sigma_u^1$) instead.

The calculated peak cross section for this channel, 1.87×10^{-19} cm^2, is smaller than the experimental value, 5.7×10^{-19} cm^2, reported by Melton [6]. The comparison with experiment is again complicated by the fact that we calculate only the two-body DEA cross section, while the available experimental data do not discriminate between production of O^-+H+H and O^-+H_2. A possible explanation for the discrepancy between our calculated results and experiment is the presence of a large three-body component to O^- production via the $^2B_2$ resonance. Rotational excitation of the target H_2O molecule, on the other hand, cannot account for this

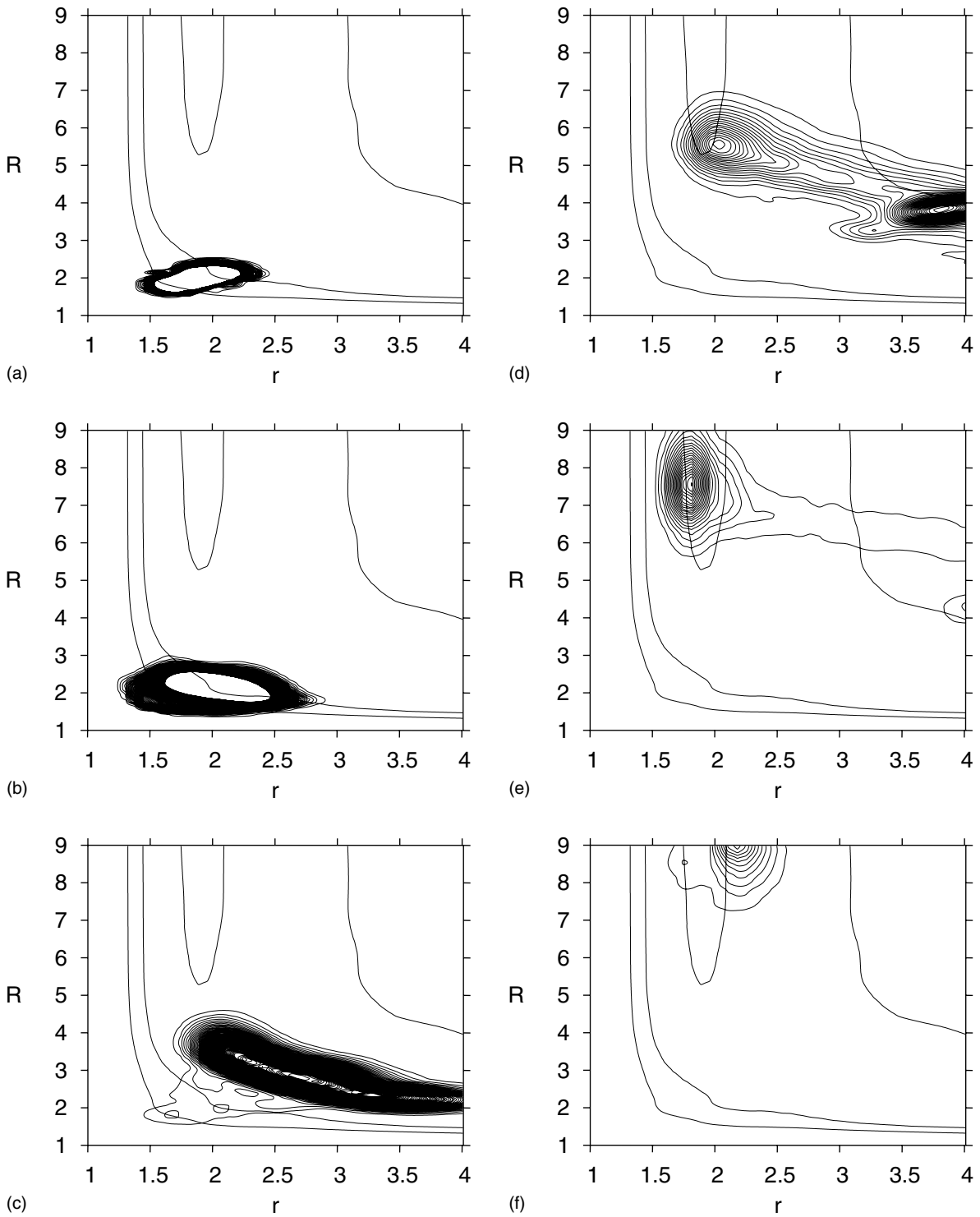

FIG. 12. Propagation of wave packet on coupled $^2B_2$ and $^2A_1$ surfaces for H^-+OH ($^2\Pi$ or $^2\Sigma$) channels, adiabatic 1 $^2A'$ ($\rightarrow^2\Pi$) component, with the real part of the 1 $^2A'$ potential-energy surface at $\gamma=90°$. Bond lengths, units of bohr. Density is integrated over γ. Propagation times, left to right and top to bottom, are 0.0, 2.0, 6.0, 10.0, 14.0, and 18.0 fs, respectively.

discrepancy. We have performed several calculations in which rotational excitation of the target is included. These include calculations for total angular momentum $J=5$, projection $K=0$. We find that the effect of such rotational excitation is minimal, as Fig. 14 shows.

We calculate a very high degree of rotational and vibrational excitation in the H_2 or D_2 fragment. The average degree of vibrational excitation $\langle\nu\rangle$ calculated from Eq. (35) is 7.75 for the H_2 fragment and 13.0 for the D_2 fragment. The corresponding values for $\langle j^2\rangle$ are 405 and 725, respectively.

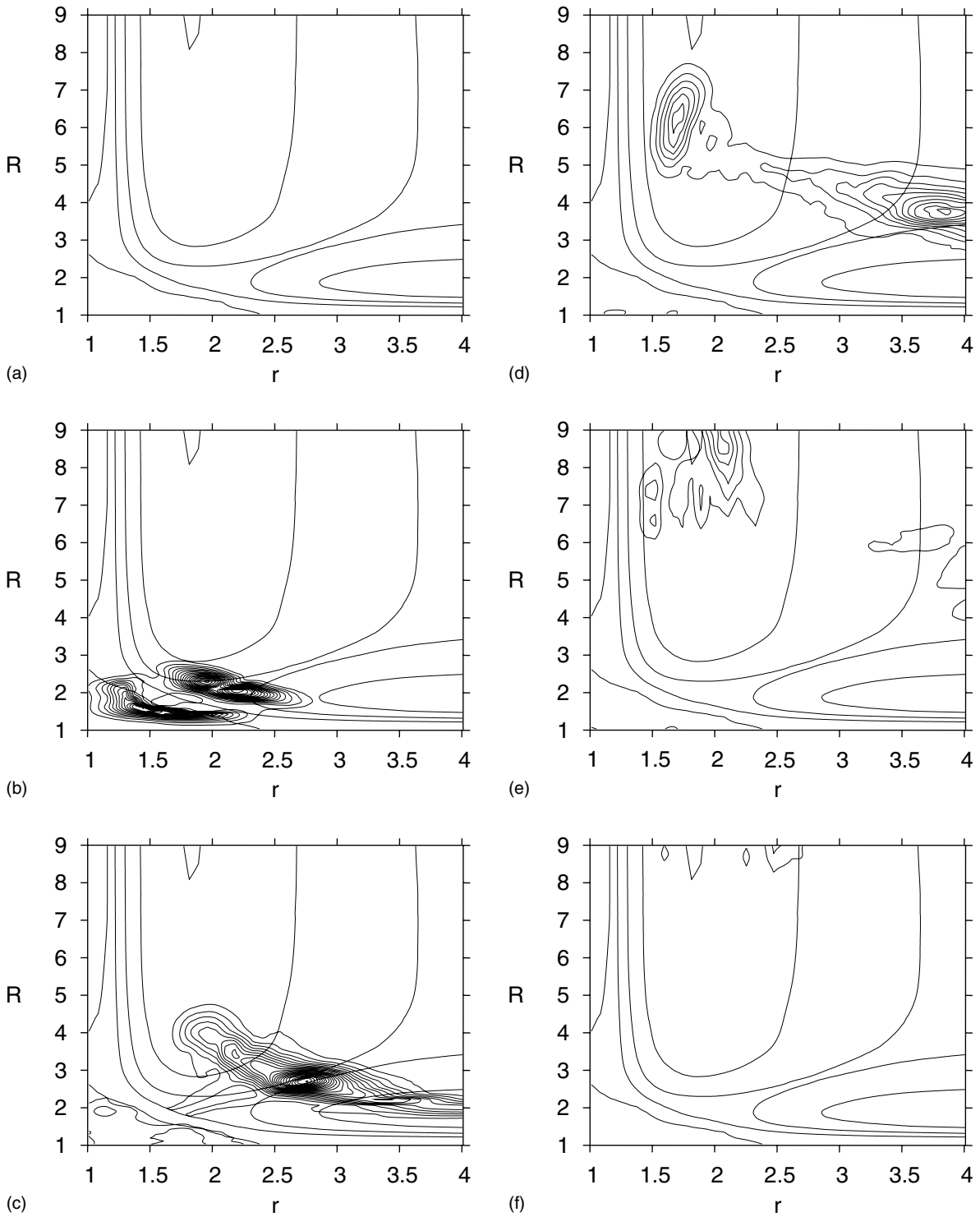

FIG. 13. Propagation of wave packet on coupled $^2B_2$ and $^2A_1$ surfaces for H^-+OH ($^2\Pi$ or $^2\Sigma$) channels, adiabatic 2 $^2A'$ ($\rightarrow^2\Sigma$) component, with the real part of the 2 $^2A'$ potential-energy surface at γ=90°. Bond lengths, units of bohr. Density is integrated over γ. Propagation times as in Fig. 12.

Figure 15 shows the total cross sections, as well as the cross sections into either rotational or vibrational states, summed over the opposite quantum number. The degree of vibrational excitation evidently increases with incident electron energy, while the degree of rotational excitation shows little correlation with incident electron energy.

The high degree of rotational and vibrational excitation of the diatomic fragment reduces the kinetic energy of the atom-diatom recoil. This is reflected in the cross sections for production of both H_2 and D_2 via the $^2B_2$ resonance, which have the greatest magnitude nearer the lower range of recoil kinetic energy. Two-dimensional plots of these cross sections

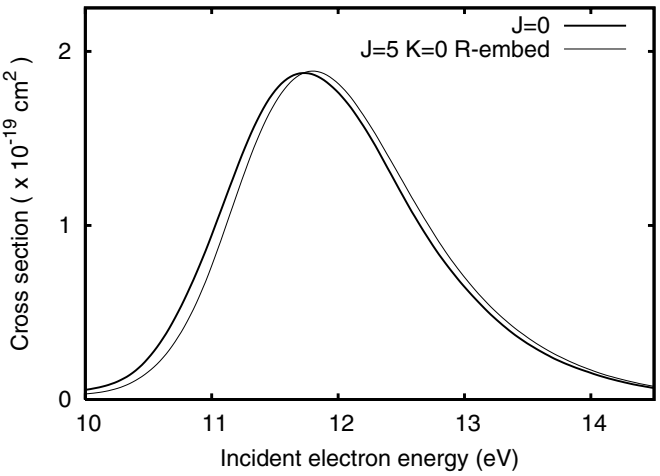

FIG. 14. Cross sections for production of $H_2(\nu)+O^-$ from $^2B_2$ state, with rotational excitation of the target, as a function of incident electron energy. Bold line, total cross sections for ground rotational state ($J=0$); thin line, calculations for $J=5$, $K=0$.

as functions of both incident electron energy and the kinetic energy of the recoil are shown in the EPAPS archive. The maximum and minimum values of available kinetic energy (assuming breakup into an atom and a H_2 molecule) are plotted as bold lines. The cross sections for H_2 and D_2 have a similar shape.

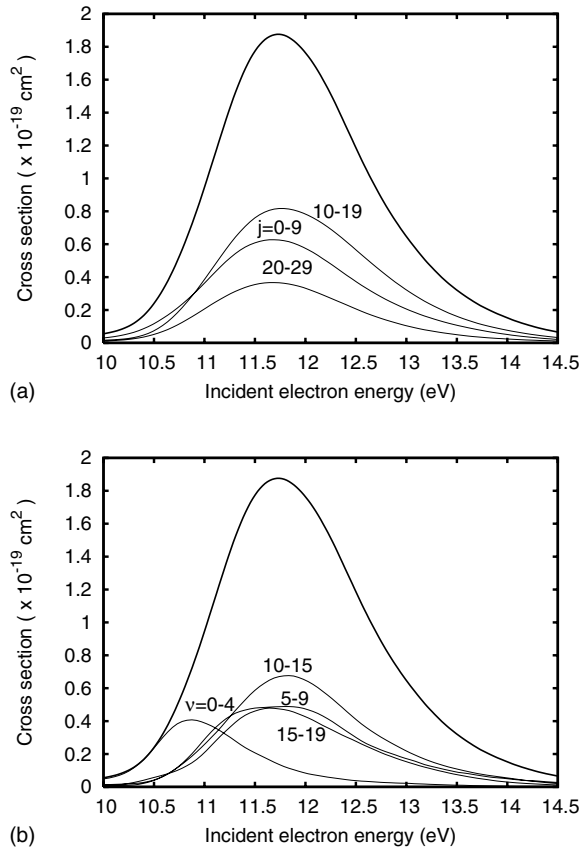

FIG. 15. Cross sections for production of $H_2(\nu)+O^-$ from $^2B_2$ state as a function of incident electron energy, showing degree of vibrational and rotational excitation of the H_2 fragment. Total cross section, thick line. Left, cross sections summed over vibrational quantum number ν and binned by rotational quantum number j; right, ν and j reversed.

Plots of the propagated wave packet for DEA via the $^2B_2$ resonance are shown in Figs. 16 and 17. The first of these shows the magnitude squared of the $1\ ^2A'$ component to the propagated wave packet, integrated over γ, and the latter shows the $2\ ^2A'$ component. The corresponding potential-energy surfaces, evaluated at $\gamma=90°$, are also plotted, along with the location of the conical intersection seam, which appears as a bold line.

The wave packet begins on the upper surface and proceeds to the lower surface only via nonadiabatic coupling near the conical intersection. As described in paper I, the gradient of the upper $2\ ^2A'$ resonance surface leads downhill toward its conical intersection with the $1\ ^2A'$ resonance, leading the propagated wave packet toward the seam. This behavior is clearly visible in Figs. 16 and 17. The $2\ ^2A'$ wave packet follows the conical intersection seam in Fig. 16, until it is consumed by the large imaginary component to that potential-energy surface and by nonadiabatic coupling to the $1\ ^2A'$ state along the intersection. The wave packet appears on the $1\ ^2A'$ surface in Fig. 17 along the conical intersection, and a small portion of it is able to reach the H_2+O^- well of that state.

The magnitude of the cross section for production of H_2+O^- from the $^2B_2$ resonance is therefore controlled by several competing effects. The shape of the real part of the potential-energy surface determines the dynamically accessible pathways and favors localization of the $2\ ^2A'$ wave packet near the conical intersection. At the same time, the large imaginary component to this surface consumes the wave packet and decreases the amount of flux available to enter the conical intersection. On the lower $1\ ^2A'$ surface, the amount of flux that enters the H_2 potential well is determined by the shape of that potential-energy surface, since the conical intersection is outside the potential well and only a fraction of the wave packet is propagated into the well.

VII. CONCLUSION

We have presented the results of a fully *ab initio* study of dissociative electron attachment to H_2O that include the full dimensionality of nuclear motion. We have attempted to calculate the cross sections for all the major and minor two-body channels that are present as asymptotes of the Born-Oppenheimer, $^2B_1$, $^2A_1$, and $^2B_2$ adiabatic electronic Feshbach resonances. While we have qualitatively described the principal features that have been experimentally observed, it is clear that a fully quantitative description of this process has yet to be achieved.

The nuclear dynamics calculations were carried out using the MCTDH method within the framework of the local complex potential model. For the major channel DEA, $H^-+OH\ (X\ ^2\Pi)$ production through the lowest $^2B_1$ resonance, the underlying assumptions of the model are well satisfied and we have obtained reasonably good agreement with the experimental observations. Another notable feature of the present study is the quantification of the mechanism in the

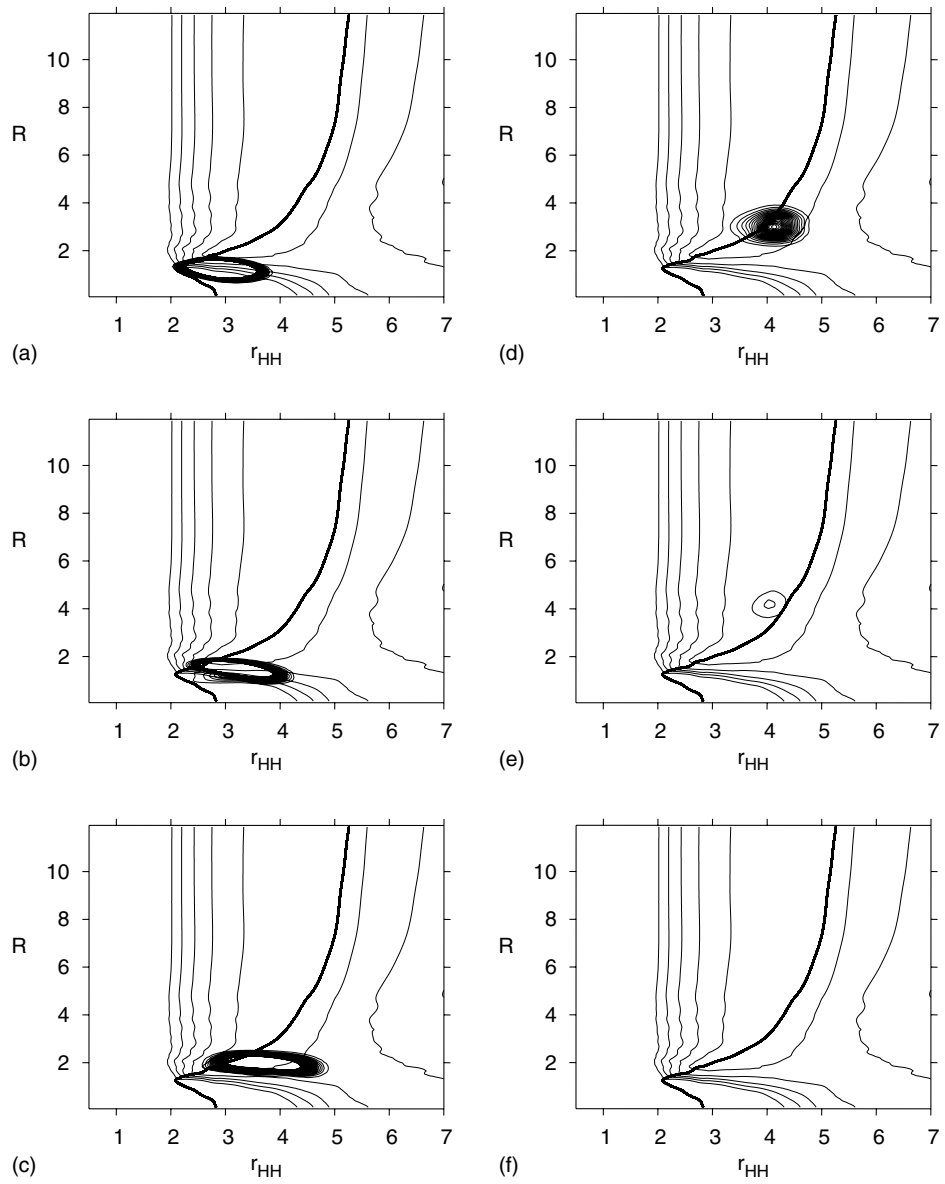

FIG. 16. Propagation on coupled $^2B_2$ and $^2A_1$ surfaces for H_2+O^- channel, adiabatic 2 $^2A'$ component. The reduced density (integrated over γ) of the adiabatic 2 $^2A'$ component of the propagated wave packet is plotted with the real part of the 2 $^2A'$ potential-energy surface at $\gamma=90°$ (C_{2v} geometry). The location of the conical intersection is marked with a bold line. Bond lengths, units of bohr. Propagation times, left to right and top to bottom, are 0.0, 2.0, 4.0, 8.0, 12.0, and 16.0 fs, respectively.

major channel that leads to production of O^- through the $^2B_1$ resonance. Our earlier speculation [18] that a conical intersection between the $^2A_1$ and $^2B_2$ states would play the key role in this process has been confirmed by the present study.

The present treatment has been limited to a consideration of DEA only into the final-state two-body channels. This limitation undoubtedly explains our inability to produce a nonzero cross section for O^- production via the $^2A_1$ resonance, which is likely to be dominated by three-body breakup. Three-body breakup may also play a role in O^- production via the $^2B_2$ resonance, and its neglect here could explain why our calculated cross sections are smaller than the experimental results, which did not differentiate two- and three-body channels.

Physics beyond the local complex potential model may be at work in some of the minor channels. Dissociative electron attachment via the $^2A_1$ Feshbach resonance may involve an even greater variety of complicated resonant as well as nonresonant phenomena not described by the LCP model. A variety of effects that go beyond the LCP model could be at play in the production of H^- via $^2A_1$ Feshbach resonance, including coupling to a broader shape resonance and even nonresonant virtual state effects. The neglect of such effects could well explain our overestimation of the cross section for production of H^-+OH via the $^2A_1$ state. Even for DEA via the lowest-energy $^2B_1$ state, nonlocal physics may be important in the minor channel, which leads to H_2+O^-.

We have achieved considerable success in describing the mean features of DEA to water, clarified the mechanisms for the two-body breakup channels, and found evidence to suggest that three-body breakup to produce O^- might be important. Nonetheless, many challenges remain before a complete

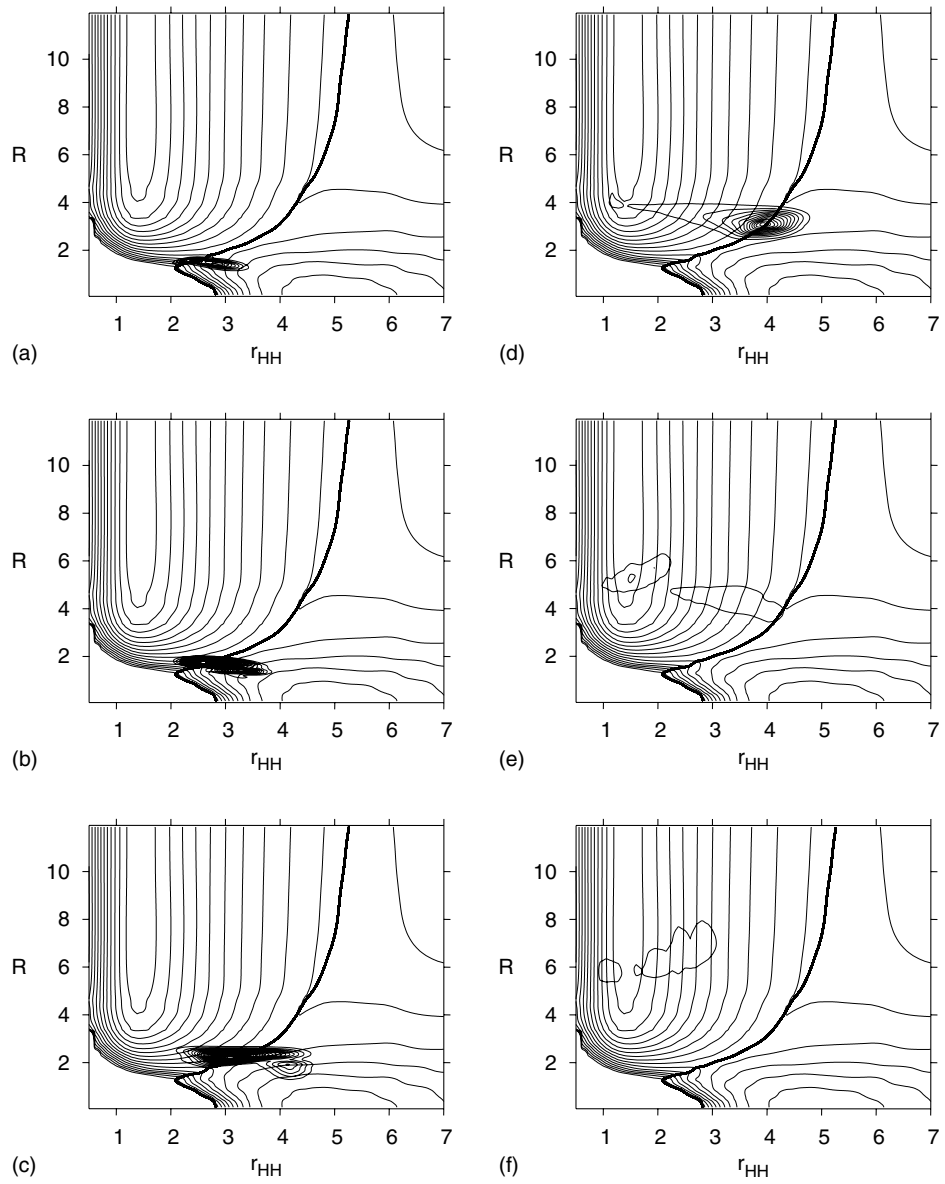

FIG. 17. Propagation on coupled $^2B_2$ and $^2A_1$ surfaces for H_2+O^- channel, adiabatic 1 $^2A'$ component. The reduced density (integrated over γ) of the adiabatic 1 $^2A'$ component of the propagated wave packet is plotted with the real part of the 1 $^2A'$ potential-energy surface at $\gamma=90°$ (C_{2v} geometry). The location of the conical intersection is marked with a bold line. Propagation times as in Fig. 16.

and quantitative understanding of this fundamental, but complicated, system will be realized.

ACKNOWLEDGMENTS

This work was performed under the auspices of the U.S. Department of Energy by the University of California Lawrence Berkeley National Laboratory under Contract No. DE-AC02-05CH11231 and was supported by the U.S. DOE Office of Basic Energy Sciences, Division of Chemical Sciences. The authors acknowledge many helpful discussions with H.-Dieter Meyer concerning various aspects of the MCTDH method.

[1] D. J. Haxton, C. W. McCurdy and T. N. Rescigno, preceding paper, Phys. Rev. A **75**, 012710 (2007).
[2] W. N. Lozier, Phys. Rev. **36**, 1417 (1930).
[3] I. S. Buchel'nikova, Zh. Eksp. Teor. Fiz. **35**, 1119 (1959).
[4] G. J. Schultz, J. Chem. Phys. **44**, 3856 (1966).
[5] R. N. Compton and L. G. Christophorou, Phys. Rev. **154**, 110 (1967).
[6] C. E. Melton, J. Chem. Phys. **57**, 4218 (1972).

[7] L. Sanche and G. J. Schultz, J. Chem. Phys. **58**, 479 (1972).
[8] S. Trajmar and R. I. Hall, J. Phys. B **7**, L458 (1974).
[9] D. S. Belić, M. Landau, and R. I. Hall, J. Phys. B **14**, 175 (1981).
[10] M. G. Curtis and I. C. Walker, J. Chem. Soc., Faraday Trans. **88**, 2805 (1992).
[11] C. R. Claydon, G. A. Segal, and H. S. Taylor, J. Chem. Phys. **54**, 3799 (1971).
[12] M. Jungen, J. Vogt, and V. Staemmler, Chem. Phys. **37**, 49 (1979).
[13] T. J. Gil, T. N. Rescigno, C. W. McCurdy, and B. H. Lengsfield III, Phys. Rev. A **49**, 2642 (1994).
[14] L. A. Morgan, J. Phys. B **31**, 5003 (1998).
[15] J. D. Gorfinkel, L. A. Morgan, and J. Tennyson, J. Phys. B **35**, 543 (2002).
[16] D. J. Haxton, Z. Zhang, C. W. McCurdy, and T. N. Rescigno, Phys. Rev. A **69**, 062713 (2003).
[17] D. J. Haxton, Z. Zhang, H.-D. Meyer, T. N. Rescigno, and C. W. McCurdy, Phys. Rev. A **69**, 062714 (2003).
[18] D. J. Haxton, T. N. Rescigno, and C. W. McCurdy, Phys. Rev. A **72**, 022705 (2005).
[19] D. J. Haxton, C. W. McCurdy, and T. N. Rescigno, Phys. Rev. A **73**, 062724 (2006).
[20] J. Fedor *et al.*, J. Phys. B **39**, 3935 (2006).
[21] D. T. Birtwistle and A. Herzenberg, J. Phys. B **4**, 53 (1971).
[22] L. Dube and A. Herzenberg, Phys. Rev. A **20**, 194 (1979).
[23] J. N. Bardsley and J. M. Wadehra, J. Chem. Phys. **78**, 7227 (1983).
[24] T. F. O'Malley and H. S. Taylor, Phys. Rev. **176**, 207 (1968).
[25] T. F. O'Malley, Phys. Rev. **150**, 14 (1966).
[26] C. E. Klots and R. N. Compton, J. Chem. Phys. **69**, 1644 (1978).
[27] S. Goursaud, M. Sizun, and F. Fiquet-Fayard, J. Chem. Phys. **65**, 5453 (1976).
[28] S. Goursaud, M. Sizun, and F. Fiquet-Fayard, J. Chem. Phys. **68**, 4310 (1978).
[29] H. Feshbach, Ann. Phys. (N.Y.) **19**, 287 (1962).
[30] J. Bieniek, J. Phys. B **13**, 4405 (1980).
[31] A. U. Hazi, T. N. Rescigno, and M. Kurilla, Phys. Rev. A **23**, 1089 (1981).
[32] C. W. McCurdy and J. L. Turner, J. Chem. Phys. **78**, 6773 (1983).
[33] J. Tennyson and B. T. Sutcliffe, J. Chem. Phys. **77**, 4061 (1982).
[34] J. Z. H. Zhang, *Theory and Application of Quantum Molecular Dynamics* (World Scientific, Sigapore, 1999).
[35] A. R. Edmonds, *Angular Momentum in Quantum Mechanics* (Princeton University Press, Princeton, NJ, 1996).
[36] C. Petrongolo, J. Chem. Phys. **89**, 1297 (1988).
[37] S. Sukiasyan and H.-D. Meyer, J. Phys. Chem. A **105**, 2604 (2001).
[38] T. Mulloney and G. C. Schatz, Chem. Phys. **45**, 213 (1980).
[39] R. T. Pack, Chem. Phys. Lett. **108**, 333 (1984).
[40] R. Renner, Z. Phys. **92**, 172 (1934).
[41] C. Jungen and A. J. Merer, Mol. Phys. **40**, 1 (1980).
[42] S. Carter and N. C. Handy, Mol. Phys. **52**, 1367 (1984).
[43] A. Loettgers, A. Untch, H.-M. Keller, R. Schinke, H.-J. Werner, C. Bauer, and P. Rosmus, J. Chem. Phys. **106**, 3186 (1997).
[44] I. B. Bersuker, Chem. Rev. (Washington, D.C.) **101**, 1067 (2001).
[45] A. V. Fishchuk, P. E. S. Wormer, and A. van der Avoird, J. Phys. Chem. A **110**, 5273 (2006).
[46] A. V. Fishchuk, G. C. Groenenboom, and A. van der Avoird, J. Phys. Chem. A **110**, 5280 (2006).
[47] G. C. Schatz and A. Kuppermann, J. Chem. Phys. **65**, 4642 (1975).
[48] H.-D. Meyer, U. Manthe, and L. S. Cederbaum, Chem. Phys. Lett. **165**, 73 (1990).
[49] U. Manthe, H.-D. Meyer, and L. S. Cederbaum, J. Chem. Phys. **97**, 3199 (1992).
[50] M. Beck, A. Jäckle, G. Worth, and H.-D. Meyer, Phys. Rep. **324**, 1 (2000).
[51] H.-D. Meyer and G. A. Worth, Theor. Chem. Acc. **109**, 251 (2003).
[52] G. A. Worth, M. H. Beck, A. Jäckle, and H.-D. Meyer, The MCTDH Package, Version 8.2, (2000). H.-D. Meyer, Version 8.3 (2002). See http://www.pci.uni-heidelberg.de/tc/usr/mctdh/.
[53] J. C. Light, in *Time-Dependent Quantum Molecular Dynamics*, edited by J. Broechkove and L. Lathouwers (Plenum, New York, 1992).
[54] C. Leforestier and R. E. Wyatt, J. Chem. Phys. **78**, 2334 (1983).
[55] R. Kosloff and D. Kosloff, J. Comput. Phys. **63**, 363 (1986).
[56] A. Jäckle and H.-D. Meyer, J. Chem. Phys. **105**, 6778 (1996).
[57] J. M. Rost, J. C. Griffin, B. Friedrich, and D. R. Herscbach, Phys. Rev. Lett. **68**, 1299 (1992).
[58] G. C. Corey and D. Lemoine, J. Chem. Phys. **97**, 4115 (1992).
[59] J. W. T. G. C. Corey and D. Lemoine, in *Numerical Grid Methods and Their Application to Schrödinger's Equation*, edited by C. Cerjan (Kluwer Academic Publishers, The Netherlands, 1973), pp. 1–23.
[60] See EPAPS Document No. E-PLRAAN-75-006702 for further details about the results of these calculations. For more information on EPAPS, see http://www.aip.org/pubservs/epaps.html.
[61] C. W. McCurdy, W. A. Isaacs, H.-D. Meyer, and T. N. Rescigno, Phys. Rev. A **67**, 042708 (2003).
[62] W. Vanroose, C. W. McCurdy, and T. N. Rescigno, Phys. Rev. A **68**, 052713 (2003).
[63] W. Vanroose, Z. Zhang, C. W. McCurdy, and T. N. Rescigno, Phys. Rev. Lett. **92**, 053201 (2004).